Ultrasound longitudinal-wave anisotropy estimation in muscle tissue

Naiara Korta Martiartu [1], Saulė Simutė [2], Marga B. Rominger [2], Thomas Frauenfelder [2], and Michael Jaeger [2]

[1]University Hospital Zürich and University of Bern
[2]Affiliation not available

November 8, 2023

Abstract

The velocity of ultrasound longitudinal waves (speed of sound) is emerging as a valuable biomarker for a wide range of diseases, including musculoskeletal disorders. Muscles are fiber-rich tissues that exhibit anisotropic behavior, meaning that velocities vary with the wave-propagation direction. Quantifying anisotropy is therefore essential to improve velocity estimates while providing a new metric that relates to both muscle composition and architecture. This work presents a method to estimate longitudinal-wave anisotropy in transversely isotropic tissues. We assume elliptical anisotropy and consider an experimental setup that includes a flat reflector located in front of the linear probe. Moreover, we consider transducers operating multistatically. This setup allows us to measure first-arrival reflection traveltimes. Unknown muscle parameters are the orientation angle of the anisotropy symmetry axis and the velocities along and across this axis. We derive analytical expressions for the relationship between traveltimes and anisotropy parameters, accounting for reflector inclinations. To analyze the structure of this nonlinear forward problem, we formulate the inversion statistically using the Bayesian framework. Solutions are probability density functions useful for quantifying uncertainties in parameter estimates. Using numerical examples, we demonstrate that all parameters can be well constrained when traveltimes from different reflector inclinations are combined. Results from a wide range of acquisition and medium properties show that uncertainties in velocity estimates are substantially lower than expected velocity differences in muscle. Thus, our formulation could provide accurate muscle anisotropy estimates in future clinical applications.

Toward speed-of-sound anisotropy quantification in muscle with pulse-echo ultrasound

Naiara Korta Martiartu, Saulė Simutė, Michael Jaeger, Thomas Frauenfelder, and Marga B. Rominger

***Abstract*—The velocity of ultrasound longitudinal waves (speed of sound) is emerging as a valuable biomarker for a wide range of diseases, including musculoskeletal disorders. Muscles are fiber-rich tissues that exhibit anisotropic behavior, meaning that velocities vary with the wave-propagation direction. Therefore, quantifying anisotropy is essential to improve velocity estimates while providing a new metric related to muscle composition and architecture. For the first time, this work presents a method to estimate speed-of-sound anisotropy in transversely isotropic tissues using pulse-echo ultrasound. We assume elliptical anisotropy and consider an experimental setup with a flat reflector parallel to the linear probe, with the muscle in between. This setup allows us to measure first-arrival reflection traveltimes using multistatic operation. Unknown muscle parameters are the orientation angle of the anisotropy symmetry axis and the velocities along and across this axis. We derive analytical expressions for the nonlinear relationship between traveltimes and anisotropy parameters, including reflector inclinations. These equations are exact for homogeneous media and are useful to estimate the effective average anisotropy in muscles. To analyze the structure of this forward problem, we formulate the inversion statistically using the Bayesian framework. We demonstrate that anisotropy parameters can be uniquely constrained by combining traveltimes from different reflector inclinations. Numerical results from wide-ranging acquisition and anisotropy properties show that uncertainties in velocity estimates are substantially lower than expected velocity differences in the muscle. Thus, our approach could provide meaningful muscle anisotropy estimates in future clinical applications.**

***Index Terms*—speed of sound, longitudinal waves, anisotropy, transverse isotropy, muscle, ultrasound, Bayesian inference, uncertainty quantification**

I. Introduction

Speed-of-sound estimation in tissue using ultrasound has attracted considerable attention in recent years [1]–[7]. Speed of sound refers to the propagation velocity of longitudinal waves, which are typically used for image formation in ultrasound systems. This property contains clinically relevant information about tissue composition and shows great promise as a biomarker for a wide range of diseases. Clinical applications involving longitudinal-wave velocities include, for instance, breast cancer screening [1], [8], [9], hepatic steatosis assessment [10], [11], and diagnosis of musculoskeletal disorders [12], [13].

Unlike breast and liver tissue, muscles exhibit anisotropic mechanical properties due to their fibrous structure. Velocities vary with the ultrasound wave-propagation direction, showing higher values along fiber direction than across fibers. Empirical studies in ex-vivo human and animal tissues have reported velocity differences of up to 24 m/s [14]–[18]. Hence, failure to properly account for anisotropy can result in unreliable velocity estimates. Quantifying anisotropy is clinically interesting mainly for two reasons. On the one hand, it can provide improved velocity estimates, which are informative about muscle composition [13]. On the other hand, this property is directly related to the muscle fiber distribution, encoding also information about muscle architecture.

Anisotropy estimation can be particularly relevant for monitoring sarcopenia cost-efficiently. This is an age-related musculoskeletal disorder characterized by the progressive loss of both muscle mass and function. Speed of sound is strongly correlated to reference standards for quantifying muscle mass loss [13] and have proven promising for differentiating young and older populations [12]. However, the loss in muscle mass is not correlated to the loss in muscle function [19], and both are required to assess this pathology accurately [20]. Current standards to measure muscle function, which is related to the muscle fiber arrangement [21], are based on questionnaires or tests [20]; thus, they do not include any quantitative imaging tool. In this context, estimating speed-of-sound anisotropy with ultrasound could bring significant benefits for assessing sarcopenia.

Methods to characterize the anisotropy of (quasi-)longitudinal waves are relatively unexplored in the literature. Studies addressing this topic have only focused on in-vitro measurements, where experimental setups are not appropriate for clinical examinations [14]–[18]. Characterization of anisotropy in shear waves, on the contrary, is an active research field. Lee et al. [22] developed an approach termed elastic tensor imaging (ETI) to map myocardial fiber directions based on shear-wave anisotropy. ETI uses either linear-probe rotations or 2D matrix-array probes [23] to measure shear-wave velocities at different propagation directions. From here, fiber orientation angles can be extracted by assuming the medium as transversely isotropic. Measurements in animal myocardial samples have demonstrated strong correlations of ETI with histological data [22] and diffusion tensor magnetic resonance

Naiara Korta Martiartu was with the Zurich Ultrasound Research and Translation (ZURT) group, Institute of Diagnostic and Interventional Radiology, University Hospital Zürich, Zürich CH-8091, Switzerland, and is now with the Institute of Applied Physics, University of Bern CH-3012, Switzerland (e-mail: naiara.korta@unibe.ch).

Saulė Simutė was with the Department of Earth Sciences, ETH Zurich, Zurich CH-8092, Switzerland.

Michael Jaeger is with the Institute of Applied Physics, University of Bern CH-3012, Switzerland.

Thomas Frauenfelder, and Marga B. Rominger are with the ZURT group, Institute of Diagnostic and Interventional Radiology, University Hospital Zürich, Zürich CH-8091, Switzerland.

imaging [24]. A similar approach using 2D matrix probes was also suggested by Wang et al. [25], who generalized the method to cases in which the shear-wave excitation push is not perpendicular to fibers. Shear-wave velocity measurements, however, are prone to artifacts caused by tissue inhomogeneities. To circumvent this, Hossain et al. [26] proposed measuring tissue peak displacements at locations of the shear-wave excitation source. Variations of this quantity as a function of the probe orientation was seen to correlate with anisotropy in shear moduli [26]. This approach showed promising results, for example, for monitoring the status of renal transplant in humans [27].

Shear and longitudinal waves interrogate fundamentally different but complementary mechanical tissue properties [28]. Due to the acquisition setup of ultrasound systems, they typically propagate in approximately perpendicular directions; thus, we cannot directly extrapolate to longitudinal waves the techniques developed for quantifying shear-wave anisotropy. This work aims to present a method capable of quantifying speed-of-sound anisotropy in muscle using pulse-echo ultrasound. We consider a setup with a flat reflector located opposite the ultrasound probe, allowing us to measure first-arrival reflection traveltimes [4]. In section II, we derive the analytical expression of the relationship between these traveltimes and muscle anisotropy. Their sensitivity to different anisotropy parameters is discussed in section III. Section IV briefly introduces the Bayesian inversion approach used in this study. We then analyze the nature of the proposed problem with various numerical examples in section V. Finally, section VI summarizes key aspects of the method and carefully discusses its clinical relevance and potential improvements.

II. Traveltime modelling in anisotropic media

The alignment of fibers in muscles causes anisotropy in mechanical muscle properties. Commonly, muscle tissue is described as a transversely isotropic medium with the symmetry axis along the fiber direction [25], [26], [29], [30]. Such a medium is characterized by five independent elastic parameters, describing, for instance, the longitudinal- and shear-wave velocities along and across the symmetry axis. In soft tissue, however, shear-wave velocities are negligible in comparison to longitudinal-wave velocities [31]. Therefore, it is possible to describe muscle properties using only three independent parameters. In this study, we assume elliptical anisotropy, which is a special case of transverse isotropy. The validity of this assumption is discussed in Appendix A. The three independent parameters are then the orientation angle φ of the anisotropy symmetry axis and the velocities along (v_1) and across (v_2) this axis. In such a medium, the group (ray) velocity $v(\theta)$ in an arbitrary propagation direction θ satisfies [32], [33]

$$\frac{v^2(\theta)}{v_1^2}\sin^2(\theta-\varphi)+\frac{v^2(\theta)}{v_2^2}\cos^2(\theta-\varphi)=1, \tag{1}$$

where the angles θ and φ are illustrated in Fig.1(a).

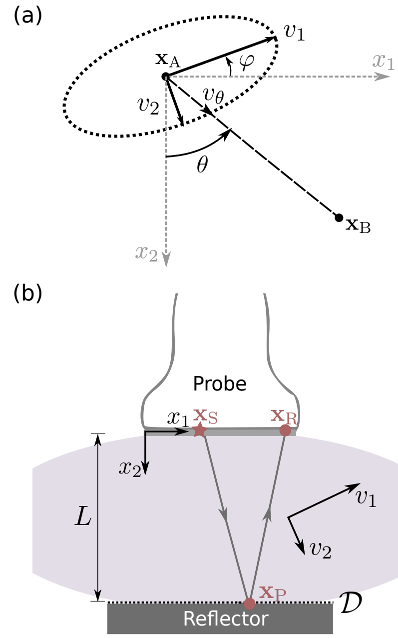

Fig. 1. Schematic representation of the anisotropic medium and experimental setup considered in this study. (a) Wavefronts in elliptically anisotropic media are ellipsoidal. Parameters v_1 and v_2 represent velocities along and across muscle fibers, and φ describes the orientation of fibers with respect to the coordinate system. In an arbitrary propagation direction θ connecting $\mathbf{x}_A$ and $\mathbf{x}_B$, waves propagate with velocity $v_\theta = v(\theta)$. (b) Our experimental setup includes a flat reflector located opposite the probe, with tissue in between. The probe-reflector distance L is assumed to be controlled by a positioning frame and a digital sensor. We measure first-arrival reflection traveltimes of ultrasound signals emitted from $\mathbf{x}_S$ and received at $\mathbf{x}_R$, with $\mathbf{x}_P \in \mathcal{D}$ indicating the reflection point.

Traveltimes of different arrivals are affected by the direction-dependent velocity $v(\theta)$, and we can use them to retrieve anisotropy parameters $\mathbf{m} = (v_1, v_2, \varphi)$. For simplicity, we consider the muscle as a two-dimensional homogeneous medium. Using (1) and trigonometric identities, the traveltime t_{AB} between positions $\mathbf{x}_A$ and $\mathbf{x}_B$ is given by

$$\begin{aligned} t_{\mathrm{AB}}^2 = &\frac{1}{v_1^2}\left[(x_{1,\mathrm{B}}-x_{1,\mathrm{A}})\cos\varphi-(x_{2,\mathrm{B}}-x_{2,\mathrm{A}})\sin\varphi\right]^2+ \\ &\frac{1}{v_2^2}\left[(x_{1,\mathrm{B}}-x_{1,\mathrm{A}})\sin\varphi+(x_{2,\mathrm{B}}-x_{2,\mathrm{A}})\cos\varphi\right]^2 . \end{aligned} \tag{2}$$

The reader is referred to the supplementary material for the detailed derivation of equations in this section. From (2) we observe that t_{AB} is nonlinearly related to anisotropic parameters $\mathbf{m}$. When the orientation of the symmetry axis is known, we obtain a linear relationship between squared traveltimes t^2 and squared slownesses $1/v_1^2$ and $1/v_2^2$.

A. Reflector-based experimental setup

This study considers an experimental setup that includes a reflector located opposite the linear ultrasound probe [see Fig. 1(b)], with the probe-reflector distance L controlled by a positioning frame and a distance sensor [4]. This setup has already been applied in various clinical studies for the assessment of breast [34], [35] and muscle tissue [12], [13],

[31], [36]. The reflector allows us to measure first-arrival reflection traveltimes t_{SR} of waves propagating from a source at x_S to a receiver at x_R. They can be expressed using Fermat's principle as

$$\min_{x_P \in D} t_{SR}(x_P); \quad \text{where} \quad t_{SR}(x_P) = t_{SP}(x_P) + t_{PR}(x_P); \quad (3)$$

where D refers to the set of points x_P at the reflector-tissue interface [see Fig. 1(b)], and traveltimes of each path are computed using (2).

Unlike in isotropic media, the reflection point x_P^{min} for the minimum traveltime does not necessarily lie on the mid-point between x_S and x_R in anisotropic media. It is possible to show that the location of the reflection point generally satisfies $x_P^{min} = ((x_{1;S} + x_{1;R})/2 + \Delta; L)$, where Δ is a constant value. That is, x_P^{min} is shifted from the source-receiver midpoint position by the same constant for every source-receiver combination. To find the value of Δ, we consider, for simplicity, the zero-offset case in which $x_S = x_R$, and we solve (3) using

$$\left.\frac{dt_{SR}}{dx_{1;P}}\right|_{x_P = x_P^{min}} = 2\left.\frac{dt_{SP}}{d\Delta}\right|_{x_P = x_P^{min}} = 0: \quad (4)$$

The reflection point is then

$$x_P^{min} = \left(\frac{x_{1;S} + x_{1;R}}{2} + \frac{L \sin 2\varphi\,(v_2^2 - v_1^2)}{2(v_1^2 \sin^2\varphi + v_2^2 \cos^2\varphi)}; L\right): \quad (5)$$

This point is located at the source-receiver midpoint only when the medium is isotropic ($v_1 = v_2$) or the anisotropy symmetry axis is aligned with our coordinate system ($\varphi = 0^\circ$). For muscle tissue, we expect $v_1 > v_2$ for $\varphi \in [-\pi/4; \pi/4]$, i.e., waves propagating faster along than across fiber direction [14]. Therefore, Δ can be either positive or negative depending on the sign of φ.

Upon inserting (5) in (3) and (2), we can observe that the path with the minimum traveltime satisfies $t_{SP}(x_P^{min}) = t_{PR}(x_P^{min})$. Therefore, the fastest ray path is the path with equal traveltime along each segment. This also means that the mirror image of the receiver, namely a virtual equivalent receiver $\tilde{R}$ below the reflector satisfying $t_{S\tilde{R}} = t_{SR}$, is located at $x_{\tilde{R}} = 2(x_P^{min} - x_S) + x_S = 2x_P^{min} - x_S$. The first-arrival reflection traveltime between x_S and x_R is then

$$t_{SR}^2(x_P^{min}) = \frac{d^2}{v^2(\theta = \pi/2)} + \frac{4L^2 v^2(\theta = \pi/2)}{v_1^2 v_2^2}; \quad (6)$$

with $v^2(\theta = \pi/2)$ given by (1) and $d = x_{1;R} - x_{1;S}$ being the source-receiver offset. This equation establishes the relationship between observations t_{SR} and unknown muscle properties $m = (v_1; v_2; \varphi)$. Thus, the forward problem considered in this study is nonlinear. When the anisotropy symmetry axis is aligned with the coordinate system ($\varphi = 0^\circ$), (6) reduces to

$$t_{SR}^2(x_P^{min}) = \frac{d^2}{v_1^2} + \frac{4L^2}{v_2^2}; \quad (7)$$

and, as previously observed, t_{SR}^2 becomes linearly related to squared slownesses $1/v_1^2$ and $1/v_2^2$. It is important to note that (5) and (6) are exact for any homogeneous media with elliptical anisotropy.

Fig. 2. Muscle models satisfying the conditions (8) and, thus, providing equal traveltimes. For this example, we take the reference model $\hat{m} = (1560$ m/s; 1540 m/s; $0^\circ)$ and represent equivalent models m for $\varphi \in [-45^\circ; 45^\circ]$. Because muscle models are defined by three parameters, we represent the anisotropy angle φ versus the velocity ratio v_1/v_2 for visualization. We only show models with velocities in the range of $[1300; 1800]$ m/s.

B. Non-uniqueness

In this section, we demonstrate that traveltimes satisfying (6) are not sufficient to constrain muscle properties uniquely. For notational brevity, we omit the dependency on x_P^{min} from traveltimes.

Let us assume that we measure traveltimes $t_{SR}^2(\hat{m})$ in the medium $\hat{m}$. If $t_{SR}^2(\hat{m})$ is uniquely defined by $\hat{m}$, then any other m giving the same traveltimes $t_{SR}^2(\hat{m}) = t_{SR}^2(m)$ must satisfy $\hat{m} = m$. For simplicity, we take $\hat{m} = (\hat{v}_1; \hat{v}_2; \hat{\varphi} = 0^\circ)$ and $m = (v_1; v_2; \varphi)$ and consider a single source-receiver pair. Equating (6) and (7), we see that both muscle parameters give the same traveltimes when

$$\hat{v}_1 \hat{v}_2 = v_1 v_2 \quad (8a)$$

$$v_1^2 \sin^2\varphi + v_2^2 \cos^2\varphi = \hat{v}_2^2: \quad (8b)$$

These conditions can be satisfied for $\hat{m} \neq m$ even when we exclude the intrinsic periodicity of φ (i.e., $m(\varphi) = m(\varphi + \pi)$) and the obvious symmetry of the elliptical anisotropy ($v_1 \leftrightarrow v_2$ when $\varphi \to \varphi + \pi/2$). Thus, traveltimes defined in (6) cannot uniquely constrain muscle anisotropy. Note that including multiple sources cannot resolve this non-uniqueness because the conditions (8) do not depend on source and receiver locations. As an example, Fig. 2 shows all equivalent muscle models (in terms of traveltimes) to the reference model $\hat{m} = (1560$ m/s; 1540 m/s; $0^\circ)$. We observe that specially the parameter φ is unconstrained by the forward problem in (6). Hence, we require additional types of observations.

C. Reflector inclination: sources of uncertainties as new constraints

The simplest way to constrain the anisotropy angle is by combining data acquired from multiple muscle sides. This is equivalent to rotating the tissue with respect to the probe. For in-vivo studies, however, we can only access the muscle from a single side of the anisotropy plane. To circumvent

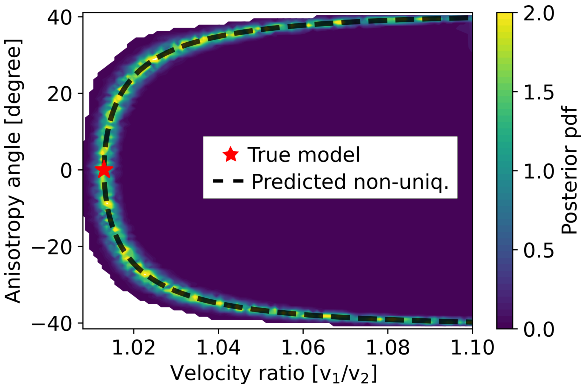

Fig. 7. Posterior probability density function (pdf) related to the unconstrained forward problem in (6). We consider 32 sources equidistantly located and the source-reflector distance $L = 8$ cm. Models with highest pdf correspond to theoretically predicted ones in Fig. 2 (dashed line). They explain equally well the traveltimes computed from the true model (red star).

the statistical information contained in the posterior using efficient sampling techniques. In this study, we employ the Metropolis-Hastings Markov chain Monte Carlo (MCMC) algorithm [45]–[47]. The algorithm generates an ensemble of random samples of the posterior with sampling density proportional to $\pi_{\text{post}}(\mathbf{m}|\mathbf{d}_{\text{obs}})$. We can use this ensemble to approximate integrals related to our statistical quantities of interest.

V. Numerical examples

In this section, we show numerical examples illustrating the nature of the anisotropy estimation problem. Our objectives are threefold: (i) show the role of the reflector inclination in constraining anisotropy parameters, (ii) investigate the robustness of the problem under uncertain inclination angles and a mistmach in probe-reflector distance between measurements, and (iii) understand the impact of the experimental setup, anisotropy properties, and measurement noise on solution uncertainties.

All examples shown here consider a uniform prior for velocities and anisotropy angle within the range of $[1300\ \text{m/s}, 1800\ \text{m/s}]$ and $[-45^\circ, 45^\circ)$, respectively. As in Section II-E, we use an ultrasound probe with 128 transducer elements and 0.3 mm pitch. We consider every fourth element acting as a source sequentially (a total of 32 sources) while all elements are in receiving mode. Following reported values in [43], where the authors compare annotated first-arrival reflection traveltimes with those estimated from reflector delineation approaches, we assume Gaussian observational errors with a standard deviation of 0.1% of maximum traveltimes. To ensure convergence and correctly interpret the statistical results, we explore the posterior with a relatively large number of random samples, $\mathcal{O}(10^7)$, although fewer samples could suffice for practical purposes.

A. Unconstrained problem

In this example, we solve the Bayesian anisotropy inference using the forward problem in (6). Our goal is to illustrate how the non-uniqueness of the forward problem is mapped into the posterior. We consider the same example as in Fig. 2, where the true model is $\mathbf{m}_{\text{true}} = (1560\ \text{m/s}, 1540\ \text{m/s}, 0^\circ)$, and the probe-reflector distance is $L = 8$ cm. Our *artificial* observations of traveltimes are numerically computed from (6) and collected in the vector $\mathbf{d}_{\text{obs}}$, which contains a total of 32×128 traveltimes. Fig. 7 shows the solution of the inverse problem, namely the posterior pdf. Models with maximum posterior probability densities are same as those theoretically predicted in Fig. 2 and explain the observations equally likely. This example demonstrates moreover that including multiple sources does not improve the non-uniqueness of (6), as previously noted. Unless our prior is stronger than a uniform distribution, the posterior will show the exact same non-uniqueness of the forward problem. In this example, however, a stronger prior would dominate the solution. For instance, a Gaussian prior would produce a maximum a posteriori point at the same location of the prior's maximum, which may not represent the true model. Hence, one should carefully interpret the posterior when the data is not informative enough on model parameters.

B. Constrained problem

We illustrate here how the problem can be constrained by combining data from multiple reflector inclinations. We consider the same true model and acquisition setup as in the previous example. Now, our artificial observables are $2 \times 32 \times 128$ traveltimes obtained with reflector inclination angles $\alpha = 0^\circ$ and $\alpha = 5^\circ$ using (12). Fig. 8(a) shows the posterior pdf for this case, which has a unique maximum that matches the true model location. Unlike the previous example, now traveltimes are able to constrain a unique set of model parameters. We can quantify uncertainties in the solution using marginal pdfs for each model parameter, shown in Fig. 8(b). Although the problem is nonlinear, the posterior pdf approximates a multivariate Gaussian distribution. We thus express the solution using the mean and standard deviation of the Gaussian fit of the marginals, which is useful to quantify uncertainties. Mean values accurately predict true model parameters with standard deviations less than 1.62 m/s for velocities and 0.61° for the anisotropy angle. As predicted in Section III, we observe that v_1 is less constrained than v_2 due to the limited aperture of the probe.

C. Uncertain reflector inclination

In Section III, we observed that traveltimes are highly sensitive to the reflector inclination angle. As a result, if we use inaccurate values of α in the forward problem, we may expect meaningless solutions. This is illustrated in Fig. 9(a), where we consider the same example as before but with errors of 5° in reflector inclination angles. That is, we fix the values of α as 5° and 10° instead of 0° and 5° to invert anisotropy parameters. The marginal pdfs show that reconstructed parameters deviate strongly from the true values. Their mean values provide a model with a negative log-posterior value of 2.74e5, meaning that there is a substantial

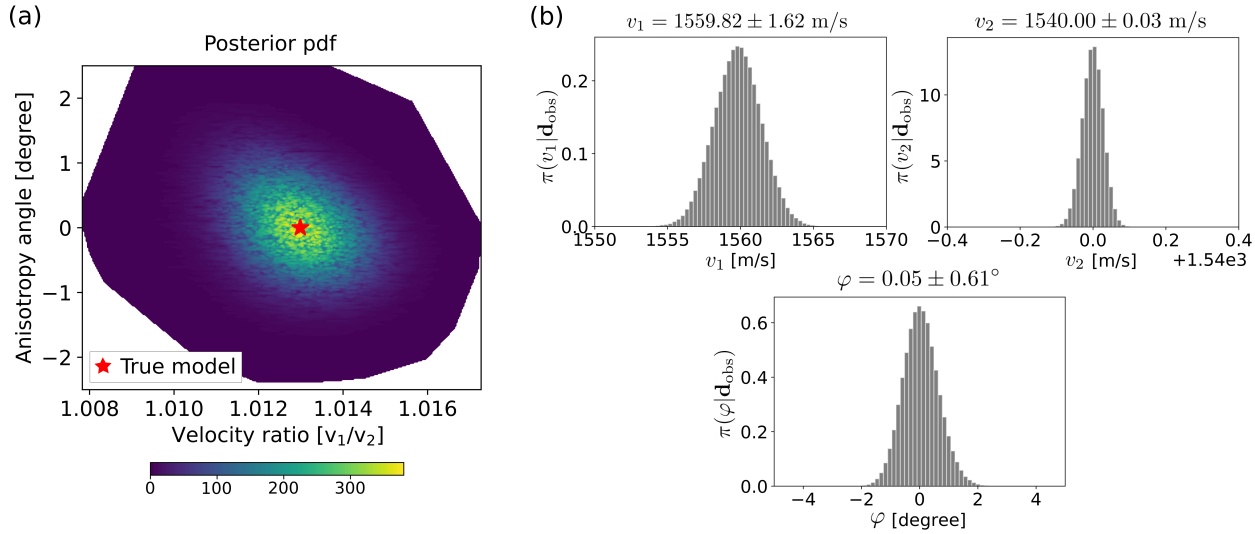

Fig. 8. (a) Posterior probability density function (pdf) when traveltimes from two different reflector inclinations (0° and 5°) are considered. We use the same true model (red star) and acquisition setup as in Fig. 7. Unsampled models by the algorithm are shown as white areas. The posterior has a unique maximum indicating that model parameters are well constrained by the traveltimes. (b) Marginal probability density functions for v_1, v_2, and φ, respectively. The marginals are histograms obtained with the Markov chain Monte Carlo algorithm and represent the sampling frequency of the values for each model parameter. The solution for each parameter is given in terms of the mean and standard deviation, shown on top of the histograms. The velocity across fibers (v_2) is better constrained than the velocity parallel to fibers (v_1).

mismatch between observed and predicted traveltimes. To circumvent this issue, we suggest extending the Bayesian formulation by including inclination angles as unknown model parameters, i.e., $\mathbf{m} = (v_1, v_2, \varphi, \alpha_1, \alpha_2)$. This also allows us to incorporate in the prior pdf our rough estimations and uncertainties of α_1 and α_2. To be consistent with the previous example, we assume Gaussian priors with means at $5°$ and $10°$ and a standard deviation of $3°$. That is, we shift Gaussian means by $5°$ from true values, with a standard deviation that excludes the true values from most probable setups. Although derivations provided in Section II-D are not sufficient to demonstrate the solution uniqueness in this case, the marginal pdfs shown in Fig. 9(b) (in gray) have a clear, unique maximum for each parameter. We show in the supplementary material that different MCMC realizations converge to the same posterior pdf, suggesting that the solution uniqueness is still given within the model subspace defined by the priors. The model based on mean values of marginal pdfs has a negative log-posterior value of 15.11; thus, it predicts observed traveltimes accurately. This result demonstrates that the anisotropy estimation is robust against uncertainties in reflector inclinations when the extended Bayesian formulation is used. The most sensitive parameters are v_2 and φ, with uncertainties that increase more than two times compared to those in Fig. 8. Furthermore, the posterior provides accurate values for α_1 and α_2, despite the substantial deviations between their prior means and true values. This indicates that the data likelihood is sufficiently informative about reflector inclination angles, as already observed in Section III. Thus, one should always consider reflector inclination angles as model parameters to retrieve meaningful anisotropy parameters.

D. Probe-reflector distance mismatch

In practice, varying the reflector inclination angle between measurements could alter the probe-reflector distance. To understand how this affects the inversion and particularly the uniqueness of the forward problem, we consider the same example as before, but with traveltimes measured using $L = 8$ cm for α_1 and $L = 7$ cm for α_2. The marginal pdfs obtained in this case are shown in pink in Fig. 9(b). Compared to our previous example, the solution is almost unaffected. Again, the mean values correctly represent the true model. However, the anisotropy angle becomes slightly more uncertain, whereas the standard deviation of v_1 is reduced. The reduced probe-reflector distance may explain the latter. In this case, the components of ray paths along v_1-direction are increased, constraining the parameter better. This result shows that a correct solution is still guaranteed when a mismatch in L exists between different reflector inclinations.

E. Impact of experimental setup, anisotropy properties, and data noise

Previous results suggest that experimental conditions influence the uncertainties of retrieved parameters. Here, we analyze these effects more in detail when the following five aspects are modified separately: the probe-reflector distance L, the true anisotropy angle φ_{true}, the true velocity differences $\Delta v_{\text{true}} = v_{1,\text{true}} - v_{2,\text{true}}$, the reflector inclination angle $\alpha_{2,\text{true}}$ while $\alpha_{1,\text{true}} = 0°$, and the standard deviation of observational errors σ_{noise}. All examples consider the reference model $\mathbf{m}_{\text{true}} = (1560 \text{ m/s}, 1540 \text{ m/s}, 0°, 0°, 5°)$ and distance $L = 8$ cm, same as in previous examples. Fig. 10 shows how the standard deviations of inverted model parameters vary in each case. As observed before, uncertainties in v_1 decrease when

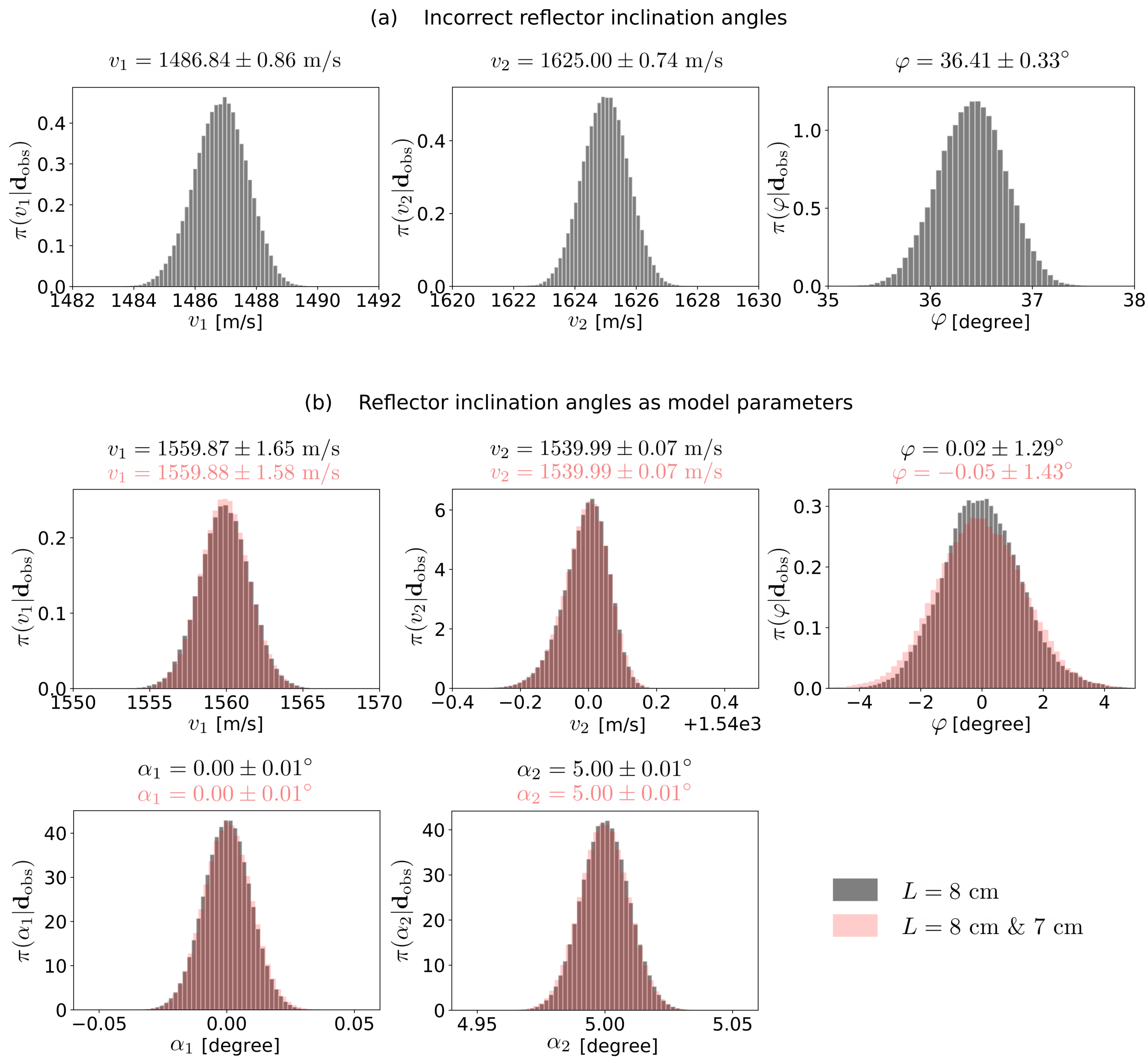

Fig. 9. Marginal probability density functions of model parameters. We use the true model $\mathbf{m}_{\text{true}} = (1560 \text{ m/s}, 1540 \text{ m/s}, 0°)$ and reflector inclination angles $0°$ and $5°$ to generate artificial observables. (a) The inversion includes an error of $5°$ in reflector inclinations. As a result, anisotropy parameters with the highest probabilities deviate strongly from true values (negative log-posterior: 2.74e5). (b) The inversion considers reflection inclination angles α_1 and α_2 as model parameters to retrieve. Inclination angles have Gaussian priors with their mean shifted $5°$ from true values and $3°$ standard deviation. In gray, we show results when probe-reflector distance L is 8 cm, same as in (a). The solution for each parameter is given in terms of the mean and standard deviation, shown on top of histograms. Mean values of marginals accurately predict true anisotropy parameters (negative log-posterior: 15.11). In pink, we show results when we use $L = 8$ cm for α_1 and $L = 7$ cm for α_2. A mismatch in L between measurements has no significant effects, and the correct solution is still guaranteed.

ray paths become closer to v_1-direction, either by decreasing L [Fig. 10(a)] or by increasing the φ_{true} [Fig. 10(b)]. The latter also increases uncertainties in v_2 due to the opposite effect of ray paths in this case. As a result, both velocities would be equally constrained when $\varphi_{\text{true}} = 45°$. Interestingly, varying Δv_{true} [Fig. 10(c)] or α_2 [Fig. 10(d)] do not affect v_1 and v_2, but φ becomes less constrained when these are small. The effect with Δv_{true} is related to the forward problem in (12), which shows that traveltimes become independent of φ when the medium is isotropic. Therefore, we expect larger uncertainties in φ when approaching isotropic conditions. The effect with α_2, on the other hand, is related to the non-uniqueness of the forward problem. As analyzed in Fig. 4, model parameters are more difficult to constrain as differences between α_1 and α_2 become smaller. When $\alpha_1 = \alpha_2$, the problem is non-unique, and φ cannot be constrained, explaining the large uncertainties in φ when $\alpha_2 \to 0$. In all these cases, standard deviations of reflector inclination angles remain constant, suggesting that they are nearly uncorrelated to other model parameters.

In general, we observe that the method is capable of accurately distinguishing velocity differences larger than 4

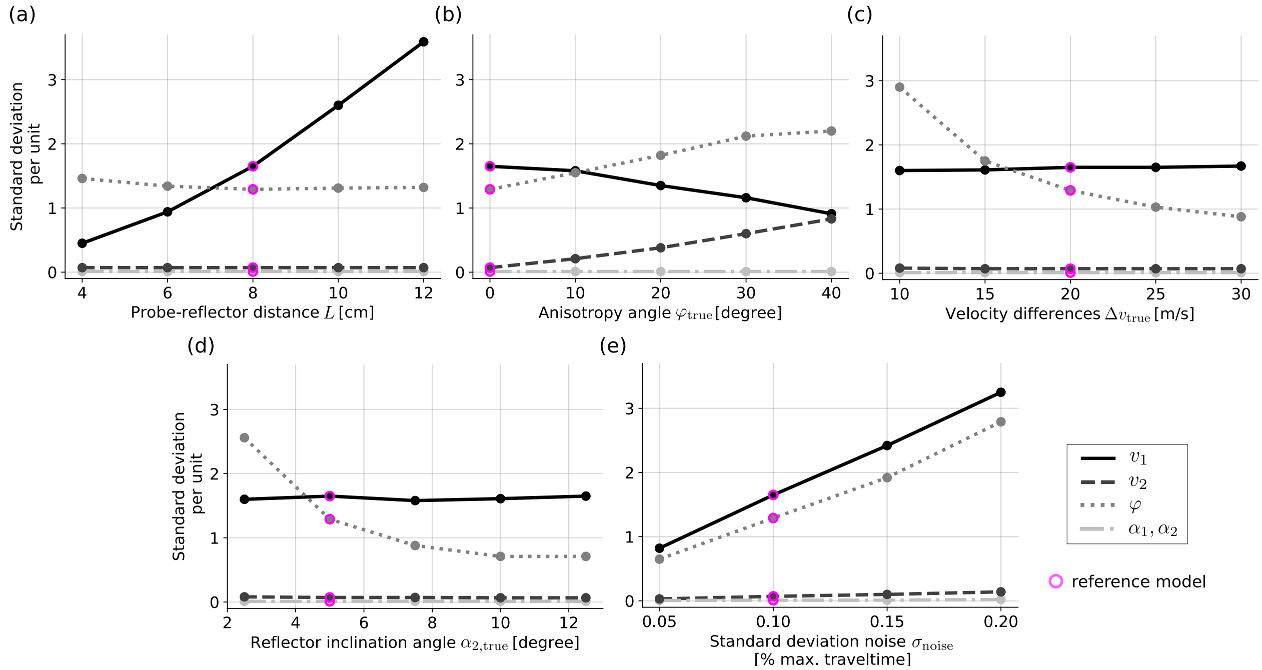

Fig. 10. Standard deviations of model parameters as a function of experimental setup, medium properties, and standard deviation of noise. The reference model and experimental parameters (pink circles) are $\mathbf{m}_{\mathrm{true}} = (1560 \text{ m/s}, 1540 \text{ m/s}, 0^\circ, 0^\circ, 5^\circ)$ and $L = 8$ cm, respectively. We modify (a) the probe-reflector distance L from 4 cm to 12 cm, (b) the true anisotropy angle φ_{true} from 0° to 40°, (c) true velocity differences $\Delta v_{\mathrm{true}} = v_{1,\mathrm{true}} - v_{2,\mathrm{true}}$ from 10 m/s to 30 m/s, (d) reflector inclination angle α from 2.5° to 12.5°, and (e) the standard deviation of traveltime observations from 0.05% to 0.2% of maximum traveltimes. In general, we can distinguish velocity differences larger than 4 m/s when the standard deviation of noise is 0.1%, as reported in [43].

m/s when observational errors are 0.1% of maximum traveltimes [43]. This is substantially smaller than velocity differences in muscle reported in the literature (> 10 m/s) [14]–[17]. Fig. 10(e) shows, however, that parameter uncertainties will increase linearly with σ_{noise}. Still, we could distiguish velocity differences larger than 10 m/s for $\sigma_{\mathrm{noise}} \leq 0.2\%$, which is a considerable increase in noise. Note moreover that uncertainties could be reduced by including more sources in our examples. Therefore, the method presented here has the potential to provide accurate and statistically meaningful muscle anisotropy estimates in future clinical applications.

VI. Discussion and Conclusions

This article presents a novel method to estimate the speed-of-sound anisotropy in transversely isotropic tissue. Until now, only shear waves have been used to characterize tissue anisotropy in clinical applications [22], [23], [25], [26], [30], [48], [49]. However, shear and longitudinal waves interrogate fundamentally different mechanical tissue properties [28]. Their propagation velocities differ by three orders of magnitude, resulting in decoupled relationships between the two velocities and elastic moduli [31]. Hence, our work not only complements other studies on the topic but is pivotal to characterize mechanical tissue properties comprehensively.

Due to the lack of previous works on tissue speed-of-sound anisotropy imaging, our work focuses on developing simplified models that provide an essential theoretical basis to understand the nature of the problem. In this respect, we target the average tissue anisotropy by modeling muscles as homogeneous media. Rather than being intrinsic, muscle anisotropy is caused by fine-scale heterogeneities in medium properties (fibers), which we implicitly consider in our formulation. However, local large-scale heterogeneities may also influence the average anisotropy estimates, hindering their interpretation. While being beyond the scope of this article, one could use the effective medium theory to establish the link between heterogeneities and anisotropy [50], [51]. From a clinical interest perspective, this link is key to correlating anisotropy parameters to muscle composition and architecture, which are affected by musculoskeletal disorders. For instance, a change in the number and type of fibers is expected to lead to changes in the average muscle anisotropy. Therefore, quantifying this property with ultrasound could ultimately provide a cost-efficient, multi-parametric biomarker to assess disease-related changes in muscle mass and function.

The method presented here relies on an experimental setup that includes a reflector parallel to the linear probe, with a sensor controlling their distance. This setup can be easily implemented in conventional ultrasound systems and has already been successfully applied in various clinical studies [12], [13], [31], [34]–[36]. Yet, it differs from those suggested for shear-wave anisotropy estimation, which requires either 2D matrix-array probes [23], [25], [49] or the rotation of linear probes around the axial direction [22], [26], [30], [48]. This difference in setups is a consequence of approximately perpendicular propagation directions of typically excited ultrasound shear and longitudinal waves. In any case, quantifying anisotropy of any kind will require redesigning current ultrasound systems.

The reflector-based setup allows us to measure arrival times of echoes reflected at known distances from the probe. One of the most important results of our work is to show that these traveltimes and anisotropy parameters are non-uniquely related. We demonstrate that anisotropy can be constrained nevertheless by combining measurements from different reflector inclinations. An inclination in the reflector is unavoidable in practice and conventionally regarded as a source of unwanted noise. Here we have resignified its value and transformed it into a key ingredient for successfully estimating anisotropy. Importantly, we show that two reflector inclinations with relatively small angle differences are sufficient to constrain anisotropy accurately. This facilitates the data acquisition procedure and avoids significant muscle deformation that could lead to changes in anisotropic properties.

Traveltimes and anisotropy parameters are nonlinearly related; accordingly, we solve the inverse problem using Bayesian inference. Compared to gradient-based optimization techniques, our choice is computationally more demanding and may not suit clinical time constraints. However, it is a powerful approach to quantify uncertainties, crucial for clinical decision-making. In the current implementation, we sample the posterior using the Metropolis-Hastings algorithm, which evaluates approximately 10^5 models per minute on a single CPU from a laptop computer with 15-20% acceptance rate. This algorithm is known to have a poor acceptance rate, meaning that a large number of samples is needed to approximate the posterior sufficiently well [52]. The performance can be significantly improved by incorporating information from derivatives of the log posterior through Hamiltonian Monte Carlo methods [52], [53]. In this way, we can guide the sampler towards high-probability regions of the model space, making the inversion computantionally more attractive.

Since traveltimes are highly sensitive to reflector inclination angles, small angular errors in the forward problem will translate to incorrect anisotropy estimates. We suggest tackling this by considering reflector inclination angles as parameters to invert. Although we could similarly include the probe-reflector distance as another unknown parameter, we consider its uncertainties negligible, following reported values (5 μm) in similar works [4]. Under this formulation, our examples show that uncertainties in velocity estimates are sufficiently low to significantly distinguish velocity differences typically observed in muscle tissue ($>$ 10 m/s) [14]–[17]. As suggested by Fig. 10(e), the validity of this conclusion closely depends on the level and nature of observational errors, which in turn depend on the applied traveltime estimation technique. Here we assume normally distributed noise, which may be justified when large measurement errors are minimized by (1) carefully selecting time intervals of expected first-arrival reflection traveltimes and (2) avoiding outliers due to cycle skips. We can satisfy these conditions with traveltime estimators based on reflector delineation approaches, commonly employed for speed-of-sound tomography [4], [43]. They are designed to remove outliers by including information on the expected reflector depth and forcing smooth traveltime variations between adjacent sensors. However, our study does not consider other sources of errors that may arise in practice (e.g., poor tissue-reflector coupling). Thus, to better understand the clinical potential of our method under realistic conditions, a Bayesian formulation integrating comprehensively and empirically characterized observational errors is required.

For nonlinear problems, the posterior pdf depends on the anisotropy model. Still, we can draw some general conclusions about uncertainties in inferred anisotropy parameters: (1) Velocities in directions more parallel to the probe (i.e., fiber direction) are generally less constrained than those in perpendicular directions due to the limited aperture of the acquisition setup. (2) The anisotropy angle φ is the least constrained parameter with relative uncertainties that are two orders of magnitudes larger than those for velocities. In fact, φ becomes increasingly unreliable as velocity differences approach isotropic conditions or the difference between reflector inclination angles becomes very small. Yet, such uncertainties do not affect velocity estimates, which encode more relevant information about tissue anisotropy. (3) Overall, the largest standard deviations in φ (3°) are substantially smaller than those reported in similar numerical studies with shear waves ($5.6^\circ - 36.3^\circ$) [23]. Maximum relative errors in velocities are also considerably lower in our case (0.2% versus 20%) [23]. It suggests that quantifying anisotropy in longitudinal waves could potentially be more robust than in shear waves.

Appendix A
Elliptical Anisotropy

This appendix discusses the elliptical anisotropy assumption in muscle and shows the conditions under which (1) is satisfied. The wave surface given by (1) is an ellipsoid only if the slowness (reciprocal of the phase velocity) surface is also an ellipsoid [32], [54]. We therefore focus on analyzing the expression for phase velocity.

For simplicity, we consider a transversely isotropic medium with the symmetry axis parallel to x_1-direction. The elastic stiffness tensor c_{ijkl} characterizing this medium has five independent components, which are $c_{1111} \equiv c_{11}$, $c_{1122} \equiv c_{12}$, $c_{2222} \equiv c_{22}$, $c_{2323} \equiv c_{44}$, and $c_{1212} \equiv c_{66}$ in Voigt notation. The parameters c_{44} and c_{66} are related to shear moduli; thus, in soft tissue, $c_{44}, c_{66} \ll c_{11}, c_{12}, c_{22}$ [29]. We can relate the stiffness tensor to phase velocities V through the Christoffel equation

$$\det[c_{ijkl}n_i n_l - \rho V^2 \delta_{jk}] = 0, \tag{20}$$

where the Einstein summation convention is implied for repeated indices. Here, ρ denotes medium density, the Kronecker delta δ_{jk} is equal to one when $j = k$ and zero otherwise, and n_i refers to the ith component of the wavefront normal vector (slowness vector). By considering a two-dimensional problem defined in the x_1x_2-plane and taking an arbitrary wavefront direction $\mathbf{n} = (\sin\phi, \cos\phi)$, (20) leads to

$$V^2(\phi) = \frac{1}{2\rho}\left[c_{11}\sin^2\phi + c_{22}\cos^2\phi + G(\phi)\right] \tag{21}$$

for longitudinal waves, with

$$G(\phi) = \left[\left(c_{11}\sin^2\phi - c_{22}\cos^2\phi\right)^2 + c_{12}^2\sin^2 2\phi\right]^{\frac{1}{2}}. \quad (22)$$

The elliptical anisotropy assumption is only valid when the slowness surface in (21) is an ellipse, which is generally not the case. Only when the medium satisfies $c_{12} = \sqrt{c_{11}c_{22}}$, (21) reduces to the ellipse

$$V^2(\phi) = \frac{1}{\rho}\left[c_{11}\sin^2\phi + c_{22}\cos^2\phi\right], \quad (23)$$

with semi-axes $\sqrt{\rho/c_{11}}$ and $\sqrt{\rho/c_{22}}$. In muscle tissue, empirical studies have shown that $c_{12} \approx \sqrt{c_{11}c_{22}}$ [29], [55], with reported deviations that are below 0.3%. This justifies the elliptical anisotropy model used in this study.

ACKNOWLEDGMENT

We gratefully acknowledge the Editor Jeremy Dahl and two anonymous reviewers for the constructive comments that substantially improved the article. The authors would also like to thank Sergio Sanabria for initial discussions and Christian Boehm for assisting with numerical wave propagation simulations. These simulations were supported by the Swiss National Supercomputing Centre (CSCS) through projects sm59 and s1040. The Python code used for generating the results of this paper can be downloaded from GitHub [56] in the form of self-explanatory Jupyter Notebooks.

REFERENCES

[1] E. A. O'Flynn, J. Fromageau, A. E. Ledger, A. Messa, A. D'Aquino, M. J. Schoemaker, M. Schmidt, N. Duric, A. J. Swerdlow, and J. C. Bamber, "Ultrasound tomography evaluation of breast density: A comparison with noncontrast magnetic resonance imaging," *Investigative Radiology*, vol. 52, no. 6, pp. 343–348, 2017.

[2] H. Gemmeke, T. Hopp, M. Zapf, C. Kaiser, and N. V. Ruiter, "3D ultrasound computer tomography: Hardware setup, reconstruction methods and first clinical results," *Nuclear Instruments and Methods in Physics Research Section A: Accelerators, Spectrometers, Detectors and Associated Equipment*, vol. 873, pp. 59–65, 2017, imaging 2016.

[3] M. Jakovljevic, S. Hsieh, R. Ali, G. Chau Loo Kung, D. Hyun, and J. J. Dahl, "Local speed of sound estimation in tissue using pulse-echo ultrasound: Model-based approach," *The Journal of the Acoustical Society of America*, vol. 144, no. 1, pp. 254–266, 2018.

[4] S. J. Sanabria, M. B. Rominger, and O. Goksel, "Speed-of-sound imaging based on reflector delineation," *IEEE Transactions on Biomedical Engineering*, vol. 66, no. 7, pp. 1949–1962, 2019.

[5] J. Wiskin, B. Malik, D. Borup, N. Pirshafiey, and J. Klock, "Full wave 3D inverse scattering transmission ultrasound tomography in the presence of high contrast," *Scientific Reports*, vol. 10, no. 1, p. 20166, 2020.

[6] N. Korta Martiartu, C. Boehm, and A. Fichtner, "3-D Wave-Equation-Based Finite-Frequency Tomography for Ultrasound Computed Tomography," *IEEE Transactions on Ultrasonics, Ferroelectrics, and Frequency Control*, vol. 67, no. 7, pp. 1332–1343, 2020.

[7] P. Stähli, M. Kuriakose, M. Frenz, and M. Jaeger, "Improved forward model for quantitative pulse-echo speed-of-sound imaging," *Ultrasonics*, vol. 108, p. 106168, 2020.

[8] G. Zografos, D. Koulocheri, P. Liakou, M. Sofras, S. Hadjiagapis, M. Orme, and V. Marmarelis, "Novel technology of multimodal ultrasound tomography detects breast lesions," *European Radiology*, vol. 23, no. 3, pp. 673–683, 2013.

[9] L. Ruby, S. J. Sanabria, K. Martini, K. J. Dedes, D. Vorburger, E. Oezkan, T. Frauenfelder, O. Goksel, and M. B. Rominger, "Breast cancer assessment with pulse-echo speed of sound ultrasound from intrinsic tissue reflections: Proof-of-concept," *Investigative Radiology*, vol. 54, no. 7, pp. 419–427, 2019.

[10] M. Dioguardi Burgio, M. Imbault, M. Ronot, A. Faccinetto, B. E. Van Beers, P.-E. Rautou, L. Castera, J.-L. Gennisson, M. Tanter, and V. Vilgrain, "Ultrasonic adaptive sound speed estimation for the diagnosis and quantification of hepatic steatosis: A pilot study," *Ultraschall Med*, vol. 40, no. 6, pp. 722–733, 2019.

[11] M. Imbault, A. Faccinetto, B.-F. Osmanski, A. Tissier, T. Deffieux, J.-L. Gennisson, V. Vilgrain, and M. Tanter, "Robust sound speed estimation for ultrasound-based hepatic steatosis assessment," *Physics in Medicine and Biology*, vol. 62, no. 9, pp. 3582–3598, apr 2017.

[12] S. J. Sanabria, K. Martini, G. Freystätter, L. Ruby, O. Goksel, T. Frauenfelder, and M. B. Rominger, "Speed of sound ultrasound: a pilot study on a novel technique to identify sarcopenia in seniors," *European Radiology*, vol. 29, no. 1, pp. 3–12, 2019.

[13] L. Ruby, A. Kunut, D. N. Nakhostin, F. A. Huber, T. Finkenstaedt, T. Frauenfelder, S. J. Sanabria, and M. B. Rominger, "Speed of sound ultrasound: comparison with proton density fat fraction assessed with Dixon MRI for fat content quantification of the lower extremity," *European Radiology*, vol. 30, no. 10, p. 5272, 2020.

[14] C. R. Mol and P. A. Breddels, "Ultrasound velocity in muscle," *The Journal of the Acoustical Society of America*, vol. 71, no. 2, pp. 455–461, 1982.

[15] D. E. Goldman and J. R. Richards, "Measurement of high-frequency sound velocity in mammalian soft tissues," *The Journal of the Acoustical Society of America*, vol. 26, no. 6, pp. 981–983, 1954.

[16] W. O'Brien and J. Olerud, "Ultrasonic assessment of tissue anisotropy," in *1995 IEEE Ultrasonics Symposium. Proceedings. An International Symposium*, vol. 2, 1995, pp. 1145–1148 vol.2.

[17] E. D. Verdonk, S. A. Wickline, and J. G. Miller, "Anisotropy of ultrasonic velocity and elastic properties in normal human myocardium," *The Journal of the Acoustical Society of America*, vol. 92, no. 6, pp. 3039–3050, 1992.

[18] K. A. Topp and W. D. O'Brien, "Anisotropy of ultrasonic propagation and scattering properties in fresh rat skeletal muscle in vitro," *The Journal of the Acoustical Society of America*, vol. 107, no. 2, pp. 1027–1033, 2000.

[19] B. H. Goodpaster, S. W. Park, T. B. Harris, S. B. Kritchevsky, M. Nevitt, A. V. Schwartz, E. M. Simonsick, F. A. Tylavsky, M. Visser, and f. t. H. A. S. Newman, Anne B., "The Loss of Skeletal Muscle Strength, Mass, and Quality in Older Adults: The Health, Aging and Body Composition Study," *The Journals of Gerontology: Series A*, vol. 61, no. 10, pp. 1059–1064, 10 2006.

[20] A. J. Cruz-Jentoft, G. Bahat, J. Bauer, Y. Boirie, O. Bruyère, T. Cederholm, C. Cooper, F. Landi, Y. Rolland, A. A. Sayer, S. M. Schneider, C. C. Sieber, E. Topinkova, M. Vandewoude, M. Visser, M. Zamboni, W. G. for the European Working Group on Sarcopenia in Older People 2 (EWGSOP2), and the Extended Group for EWGSOP2, "Sarcopenia: revised European consensus on definition and diagnosis," *Age and Ageing*, vol. 48, no. 1, pp. 16–31, 09 2018.

[21] M. V. Narici, C. N. Maganaris, N. D. Reeves, and P. Capodaglio, "Effect of aging on human muscle architecture," *Journal of Applied Physiology*, vol. 95, no. 6, pp. 2229–2234, 2003, pMID: 12844499.

[22] W.-N. Lee, M. Pernot, M. Couade, E. Messas, P. Bruneval, A. Bel, A. A. Hagege, M. Fink, and M. Tanter, "Mapping myocardial fiber orientation using echocardiography-based shear wave imaging," *IEEE Transactions on Medical Imaging*, vol. 31, no. 3, pp. 554–562, 2012.

[23] M. Correia, T. Deffieux, S. Chatelin, J. Provost, M. Tanter, and M. Pernot, "3D elastic tensor imaging in weakly transversely isotropic soft tissues," *Physics in Medicine & Biology*, vol. 63, no. 15, p. 155005, jul 2018.

[24] W.-N. Lee, B. Larrat, M. Pernot, and M. Tanter, "Ultrasound elastic tensor imaging: comparison with MR diffusion tensor imaging in the myocardium," *Physics in Medicine and Biology*, vol. 57, no. 16, pp. 5075–5095, jul 2012.

[25] M. Wang, B. Byram, M. Palmeri, N. Rouze, and K. Nightingale, "Imaging transverse isotropic properties of muscle by monitoring acoustic radiation force induced shear waves using a 2-D matrix ultrasound array," *IEEE Transactions on Medical Imaging*, vol. 32, no. 9, pp. 1671–1684, 2013.

[26] M. Hossain, C. J. Moore, and C. M. Gallippi, "Acoustic radiation force impulse-induced peak displacements reflect degree of anisotropy in transversely isotropic elastic materials," *IEEE Transactions on Ultrasonics, Ferroelectrics, and Frequency Control*, vol. 64, no. 6, pp. 989–1001, 2017.

[27] M. M. Hossain, R. K. Detwiler, E. H. Chang, M. C. Caughey, M. W. Fisher, T. C. Nichols, E. P. Merricks, R. A. Raymer, M. Whitford, D. A. Bellinger, L. E. Wimsey, and C. M. Gallippi, "Mechanical Anisotropy Assessment in Kidney Cortex Using ARFI Peak Displacement: Preclinical Validation and Pilot In Vivo Clinical Results in Kidney Allografts," *IEEE Transactions on Ultrasonics, Ferroelectrics, and Frequency Control*, vol. 66, no. 3, pp. 551–562, 2019.

[28] T. Glozman and H. Azhari, "A method for characterization of tissue elastic properties combining ultrasonic computed tomography with elastography," *Journal of Ultrasound in Medicine*, vol. 29, no. 3, pp. 387–398, 2010.

[29] S. F. Levinson, "Ultrasound propagation in anisotropic soft tissues: The application of linear elastic theory," *Journal of Biomechanics*, vol. 20, no. 3, pp. 251–260, 1987.

[30] J.-L. Gennisson, T. Deffieux, E. Macé, G. Montaldo, M. Fink, and M. Tanter, "Viscoelastic and anisotropic mechanical properties of in vivo muscle tissue assessed by supersonic shear imaging," *Ultrasound in Medicine & Biology*, vol. 36, no. 5, pp. 789–801, 2010.

[31] N. Korta Martiartu, D. Nakhostin, L. Ruby, T. Frauenfelder, M. B. Rominger, and S. J. Sanabria, "Speed of sound and shear wave speed for calf soft tissue composition and nonlinearity assessment," *Quantitative Imaging in Medicine and Surgery*, vol. 11, no. 9, 2021.

[32] B. S. Byun, "Seismic parameters for media with elliptical velocity dependencies," *GEOPHYSICS*, vol. 47, no. 12, pp. 1621–1626, 1982.

[33] N. Korta Martiartu, S. Simute, C. Boehm, L. Ruby, T. Frauenfelder, A. Fichtner, M. Rominger, and S. J. Sanabria, "Speed-of-sound anisotropy estimation using reflector-based pulse-echo ultrasound," in *Medical Imaging 2021: Ultrasonic Imaging and Tomography*, B. C. Byram and N. V. Ruiter, Eds., vol. 11602, International Society for Optics and Photonics. SPIE, 2021.

[34] S. J. Sanabria, O. Goksel, K. Martini, S. Forte, T. Frauenfelder, R. A. Kubik-Huch, and M. B. Rominger, "Breast-density assessment with hand-held ultrasound: A novel biomarker to assess breast cancer risk and to tailor screening?" *European Radiology*, vol. 28, no. 8, pp. 3165–3175, 2018.

[35] L. Ruby, S. J. Sanabria, A. S. Obrist, K. Martini, S. Forte, O. Goksel, T. Frauenfelder, R. A. Kubik-Huch, and M. B. Rominger, "Breast density assessment in young women with ultrasound based on speed of sound: Influence of the menstrual cycle," *Medicine*, vol. 98, no. 25, p. e16123, 2019.

[36] L. Ruby, S. J. Sanabria, K. Martini, T. Frauenfelder, G. N. Jukema, O. Goksel, and M. B. Rominger, "Quantification of immobilization-induced changes in human calf muscle using speed-of-sound ultrasound: An observational pilot study," *Medicine*, vol. 100, no. 10, p. e23576, 2021.

[37] S. J. Sanabria and O. Goksel, "Hand-held sound-speed imaging based on ultrasound reflector delineation," in *Medical Image Computing and Computer-Assisted Intervention – MICCAI 2016*, S. Ourselin, L. Joskowicz, M. R. Sabuncu, G. Unal, and W. Wells, Eds. Cham: Springer International Publishing, 2016, pp. 568–576.

[38] M. Afanasiev, C. Boehm, M. van Driel, L. Krischer, M. Rietmann, D. A. May, M. G. Knepley, and A. Fichtner, "Modular and flexible spectral-element waveform modelling in two and three dimensions," *Geophysical Journal International*, vol. 216, no. 3, pp. 1675–1692, 11 2018.

[39] A. Tarantola, *Inverse Problem Theory and Methods for Model Parameter Estimation*. Society for Industrial and Applied Mathematics, 2005.

[40] K. Mosegaard and A. Tarantola, "Monte Carlo sampling of solutions to inverse problems," *Journal of Geophysical Research: Solid Earth*, vol. 100, no. B7, pp. 12 431–12 447, 1995.

[41] T. Bayes and R. Price, "An essay towards solving a problem in the doctrine of chances," *Philosophical Transactions of the Royal Society of London*, vol. 53, pp. 370–418, 1763.

[42] A. Tarantola and B. Valetter, "Inverse Problems = Quest for Information," *Journal of Geophysics*, vol. 50, no. 1, pp. 159–170, 1982.

[43] B. R. Chintada, R. Rau, and O. Goksel, "Time of arrival delineation in echo traces for reflection ultrasound tomography," in *2021 IEEE 18th International Symposium on Biomedical Imaging (ISBI)*, 2021, pp. 1342–1345.

[44] N. Korta Martiartu, C. Boehm, V. Hapla, H. Maurer, I. J. Balic, and A. Fichtner, "Optimal experimental design for joint reflection-transmission ultrasound breast imaging: From ray- to wave-based methods," *The Journal of the Acoustical Society of America*, vol. 146, no. 2, pp. 1252–1264, 2019.

[45] N. Metropolis, A. W. Rosenbluth, M. N. Rosenbluth, A. H. Teller, and E. Teller, "Equation of state calculations by fast computing machines," *The Journal of Chemical Physics*, vol. 21, no. 6, pp. 1087–1092, 1953.

[46] W. K. Hastings, "Monte Carlo Sampling Methods Using Markov Chains and Their Applications," *Biometrika*, vol. 57, no. 1, pp. 97–109, 1970.

[47] L. Tierney, "Markov Chains for Exploring Posterior Distributions," *The Annals of Statistics*, vol. 22, no. 4, pp. 1701 – 1728, 1994.

[48] J.-L. Gennisson, S. Catheline, S. Chaffaï, and M. Fink, "Transient elastography in anisotropic medium: Application to the measurement of slow and fast shear wave speeds in muscles," *The Journal of the Acoustical Society of America*, vol. 114, no. 1, pp. 536–541, 2003.

[49] M. M. Hossain and C. M. Gallippi, "Electronic Point Spread Function Rotation Using a Three-Row Transducer for ARFI-Based Elastic Anisotropy Assessment: In Silico and Experimental Demonstration," *IEEE Transactions on Ultrasonics, Ferroelectrics, and Frequency Control*, vol. 68, no. 3, pp. 632–646, 2021.

[50] G. E. Backus, "Long-wave elastic anisotropy produced by horizontal layering," *Journal of Geophysical Research (1896-1977)*, vol. 67, no. 11, pp. 4427–4440, 1962.

[51] T. H. Jordan, "An effective medium theory for three-dimensional elastic heterogeneities," *Geophysical Journal International*, vol. 203, no. 2, pp. 1343–1354, 10 2015.

[52] M. Betancourt, "A Conceptual Introduction to Hamiltonian Monte Carlo," 2018.

[53] S. Duane, A. Kennedy, B. J. Pendleton, and D. Roweth, "Hybrid Monte Carlo," *Physics Letters B*, vol. 195, no. 2, pp. 216–222, 1987.

[54] K. Helbig, "Elliptical anisotropy—its significance and meaning," *GEOPHYSICS*, vol. 48, no. 7, pp. 825–832, 1983.

[55] D. Royer, J.-L. Gennisson, T. Deffieux, and M. Tanter, "On the elasticity of transverse isotropic soft tissues (l)," *The Journal of the Acoustical Society of America*, vol. 129, no. 5, pp. 2757–2760, 2011.

[56] N. Korta Martiartu, "MCMC SoS anisotropy estimation with pulse-echo ultrasound," 2 2022. [Online]. Available: https://github.com/naiarako/UltrasoundAnisotropy

Supplementary material for "Toward speed-of-sound anisotropy quantification in muscle with pulse-echo ultrasound"

Naiara Korta Martiartu, Saulė Simutė, Michael Jaeger, Thomas Frauenfelder, and Marga B. Rominger

I. Content

This supplementary material shows the detailed derivation of equations summarized in the main manuscript and figures clarifying the results shown in Figs. 4 and 9b.

II. Traveltimes in elliptically anisotropic media

In a medium with elliptical anisotropy, the group velocity of longitudinal waves $v(\theta)$ in an arbitrary propagation direction θ satisfies

$$\frac{v^2(\theta)}{v_1^2}\sin^2(\theta-\varphi)+\frac{v^2(\theta)}{v_2^2}\cos^2(\theta-\varphi)=1, \tag{1}$$

where v_1 and v_2 are the longitudinal-wave velocities along and across the anisotropy symmetry axis, respectively, and the angle φ indicates the orientation of this axis with respect to our reference system [see Fig. 1(a) in the main manuscript]. Equivalently, we can rewrite this equation as

$$\frac{1}{v^2(\theta)}=\frac{1}{v_1^2}\sin^2(\theta-\varphi)+\frac{1}{v_2^2}\cos^2(\theta-\varphi) \tag{2}$$

to explicitly define $v(\theta)$.

In homogeneous media, the traveltime of longitudinal waves propagating between arbitrary locations $\mathbf{x}_\mathrm{A}$ and $\mathbf{x}_\mathrm{B}$ is generally given by

$$t_\mathrm{AB}=\frac{||\mathbf{x}_\mathrm{B}-\mathbf{x}_\mathrm{A}||}{v(\theta)}, \tag{3}$$

where $||\cdot||$ refers to the Euclidean norm, and θ is the angular position of $\mathbf{x}_\mathrm{B}$ with respect our the coordinate system, with its origin at $\mathbf{x}_\mathrm{A}$ [see Fig. 1(a) in the main manuscript].

After taking the square of (3) and replacing $v(\theta)$ with the definition given in (2), we obtain

$$t_\mathrm{AB}^2=\frac{||\mathbf{x}_\mathrm{B}-\mathbf{x}_\mathrm{A}||^2}{v_1^2}\sin^2(\theta-\varphi)+\frac{||\mathbf{x}_\mathrm{B}-\mathbf{x}_\mathrm{A}||^2}{v_2^2}\cos^2(\theta-\varphi). \tag{4}$$

This equation can be simplified by applying standard trigonometric identities and using the geometric relations $||\mathbf{x}_\mathrm{B}-\mathbf{x}_\mathrm{A}||\sin\theta=x_{1,\mathrm{B}}-x_{1,\mathrm{A}}$ and $||\mathbf{x}_\mathrm{B}-\mathbf{x}_\mathrm{B}||\cos\theta=x_{2,\mathrm{B}}-x_{2,\mathrm{A}}$. Finally, we can express the traveltime t_AB as

$$t_\mathrm{AB}^2=\frac{1}{v_1^2}\left[(x_{1,\mathrm{B}}-x_{1,\mathrm{A}})\cos\varphi-(x_{2,\mathrm{B}}-x_{2,\mathrm{A}})\sin\varphi\right]^2+\frac{1}{v_2^2}\left[(x_{1,\mathrm{B}}-x_{1,\mathrm{A}})\sin\varphi+(x_{2,\mathrm{B}}-x_{2,\mathrm{A}})\cos\varphi\right]^2. \tag{5}$$

III. Reflector-based experimental setup: derivation of the reflection point

Let us consider a reflector-based experimental setup with the reflector parallel to the ultrasound probe [see Fig. 1(b) in the main manuscript]. We can use Fermat's principle to analytically derive the first-arrival reflection traveltime t_SR of waves propagating from a source at $\mathbf{x}_\mathrm{S}$ to a receiver at $\mathbf{x}_\mathrm{R}$ as

$$\min_{\mathbf{x}_\mathrm{P}\in\mathcal{D}} t_\mathrm{SR}(\mathbf{x}_\mathrm{P}),\quad \text{where}\quad t_\mathrm{SR}(\mathbf{x}_\mathrm{P})=t_\mathrm{SP}(\mathbf{x}_\mathrm{P})+t_\mathrm{PR}(\mathbf{x}_\mathrm{P}). \tag{6}$$

Here, $\mathcal{D}$ refers to the set of points $\mathbf{x}_\mathrm{P}$ at the reflector-tissue interface [see Fig. 1(b) in the main manuscript], and traveltimes of each path are computed using (5).

Naiara Korta Martiartu was with the Zurich Ultrasound Research and Translation (ZURT) group, Institute of Diagnostic and Interventional Radiology, University Hospital Zürich, Zürich CH-8091, Switzerland, and is now with the Institute of Applied Physics, University of Bern CH-3012, Switzerland (e-mail: naiara.korta@unibe.ch).

Saulė Simutė was with the Department of Earth Sciences, ETH Zurich, Zurich CH-8092, Switzerland.

Michael Jaeger is with the Institute of Applied Physics, University of Bern CH-3012, Switzerland.

Thomas Frauenfelder, and Marga B. Rominger are with the ZURT group, Institute of Diagnostic and Interventional Radiology, University Hospital Zürich, Zürich CH-8091, Switzerland.

In a first step, we compute the location of the reflection point $\mathbf{x}_{\mathrm{P}}^{\min}$ satisfying (6). We assume that this point is shifted from the source-receiver mid-point position by the same constant δ for every source-receiver combination, i.e., $\mathbf{x}_{\mathrm{P}}^{\min} = ((x_{1,\mathrm{S}} + x_{1,\mathrm{R}})/2 + \delta, L)$. To find the value of δ, we consider, for simplicity, the zero-offset case in which $\mathbf{x}_{\mathrm{S}} = \mathbf{x}_{\mathrm{R}}$, and we solve (6) using

$$\left.\frac{dt_{\mathrm{SR}}}{dx_{1,\mathrm{P}}}\right|_{\mathbf{x}_{\mathrm{P}}=\mathbf{x}_{\mathrm{P}}^{\min}} = 2\left.\frac{dt_{\mathrm{SP}}}{d\delta}\right|_{\mathbf{x}_{\mathrm{P}}=\mathbf{x}_{\mathrm{P}}^{\min}} = 0. \tag{7}$$

Because the derivative of t_{SP} with respect to δ must be zero when the reflection point is $\mathbf{x}_{\mathrm{P}}^{\min}$, the same must hold for the derivative of t_{SP}^2:

$$\left.\frac{dt_{\mathrm{SP}}^2}{d\delta}\right|_{\mathbf{x}_{\mathrm{P}}=\mathbf{x}_{\mathrm{P}}^{\min}} = 2t_{\mathrm{SP}}\left.\frac{dt_{\mathrm{SP}}}{d\delta}\right|_{\mathbf{x}_{\mathrm{P}}=\mathbf{x}_{\mathrm{P}}^{\min}} = 0, \tag{8}$$

which is easier to compute from (5). In our zero-offset case, t_{SP}^2 has the form

$$\left.t_{\mathrm{SP}}^2\right|_{\mathbf{x}_{\mathrm{S}}=\mathbf{x}_{\mathrm{R}}} = \frac{1}{v_1^2}\left[\delta\cos\varphi - L\sin\varphi\right]^2 + \frac{1}{v_2^2}\left[\delta\sin\varphi + L\cos\varphi\right]^2, \tag{9}$$

and its derivative with respect to δ is

$$\left.\frac{dt_{\mathrm{SP}}^2}{d\delta}\right|_{\mathbf{x}_{\mathrm{S}}=\mathbf{x}_{\mathrm{R}}} = \frac{2\cos\varphi}{v_1^2}\left[\delta\cos\varphi - L\sin\varphi\right] + \frac{2\sin\varphi}{v_2^2}\left[\delta\sin\varphi + L\cos\varphi\right]. \tag{10}$$

By imposing the condition (8), we find that δ satisfies

$$\delta = \frac{L\sin\varphi\cos\varphi\left[\frac{1}{v_1^2} - \frac{1}{v_2^2}\right]}{\frac{1}{v_1^2}\cos^2\varphi + \frac{1}{v_2^2}\sin^2\varphi} = \frac{L\sin 2\varphi(v_2^2 - v_1^2)}{2(v_1^2\sin^2\varphi + v_2^2\cos^2\varphi)}. \tag{11}$$

Thus, the reflection point of fastest waves propagating from $\mathbf{x}_{\mathrm{S}}$ to $\mathbf{x}_{\mathrm{R}}$ is generally given by

$$\mathbf{x}_{\mathrm{P}}^{\min} = \left(\frac{x_{1,\mathrm{S}} + x_{1,\mathrm{R}}}{2} + \frac{L\sin 2\varphi(v_2^2 - v_1^2)}{2(v_1^2\sin^2\varphi + v_2^2\cos^2\varphi)}, L\right). \tag{12}$$

IV. Reflector-based experimental setup: first-arrival reflection traveltime

The first-arrival reflection traveltime is the sum of two terms:

$$t_{\mathrm{SR}}(\mathbf{x}_{\mathrm{P}}^{\min}) = t_{\mathrm{SP}}(\mathbf{x}_{\mathrm{P}}^{\min}) + t_{\mathrm{PR}}(\mathbf{x}_{\mathrm{P}}^{\min}). \tag{13}$$

For simplicity, before computing these two traveltimes, we focus on deriving simplified expressions for their squared counterparts:

1) Traveltime from the source to the reflection point:

$$\begin{aligned} t_{\mathrm{SP}}^2\left(\mathbf{x}_{\mathrm{P}}^{\min}\right) = \frac{1}{v_1^2}&\left[\left(\frac{d}{2} + \frac{L\sin 2\varphi(v_2^2 - v_1^2)}{2(v_1^2\sin^2\varphi + v_2^2\cos^2\varphi)}\right)\cos\varphi - L\sin\varphi\right]^2 \\ &+\frac{1}{v_2^2}\left[\left(\frac{d}{2} + \frac{L\sin 2\varphi(v_2^2 - v_1^2)}{2(v_1^2\sin^2\varphi + v_2^2\cos^2\varphi)}\right)\sin\varphi + L\cos\varphi\right]^2, \end{aligned} \tag{14}$$

where $d = x_{1,\mathrm{R}} - x_{1,\mathrm{S}}$ is the source-receiver offset. The terms in brackets can be further simplified as

$$\begin{aligned} \left(\frac{d}{2} + \frac{L\sin 2\varphi(v_2^2 - v_1^2)}{2(v_1^2\sin^2\varphi + v_2^2\cos^2\varphi)}\right)\cos\varphi - L\sin\varphi &= \frac{d}{2}\cos\varphi + L\sin\varphi\left[\frac{\cos^2\varphi(v_2^2 - v_1^2) - (v_1^2\sin^2\varphi + v_2^2\cos^2\varphi)}{v_1^2\sin^2\varphi + v_2^2\cos^2\varphi}\right] \\ &= \frac{d}{2}\cos\varphi - \frac{Lv_1^2\sin\varphi}{v_1^2\sin^2\varphi + v_2^2\cos^2\varphi} \end{aligned} \tag{15}$$

and

$$\left(\frac{d}{2} + \frac{L\sin 2\varphi(v_2^2 - v_1^2)}{2(v_1^2\sin^2\varphi + v_2^2\cos^2\varphi)}\right)\sin\varphi + L\sin\varphi = \frac{d}{2}\sin\varphi + \frac{Lv_2^2\cos\varphi}{v_1^2\sin^2\varphi + v_2^2\cos^2\varphi}. \tag{16}$$

By replacing them in (14), we obtain

$$t_{\mathrm{SP}}^2\left(\mathbf{x}_{\mathrm{P}}^{\min}\right) = \frac{1}{v_1^2}\left[\frac{d}{2}\cos\varphi - \frac{Lv_1^2\sin\varphi}{v_1^2\sin^2\varphi + v_2^2\cos^2\varphi}\right]^2 + \frac{1}{v_2^2}\left[\frac{d}{2}\sin\varphi + \frac{Lv_2^2\cos\varphi}{v_1^2\sin^2\varphi + v_2^2\cos^2\varphi}\right]^2, \tag{17}$$

which reduces to

$$t_{\mathrm{SP}}^2\left(\mathbf{x}_{\mathrm{P}}^{\min}\right)=\frac{d^2}{4v_1^2v_2^2}(v_1^2\sin^2\varphi+v_2^2\cos^2\varphi)+\frac{L^2}{v_1^2\sin^2\varphi+v_2^2\cos^2\varphi}=\frac{d^2}{4v^2(\theta=\pi/2)}+\frac{L^2v^2(\theta=\pi/2)}{v_1^2v_2^2}. \tag{18}$$

We used (1) in the last step.

2) Traveltime from the reflection point to the receiver:

$$\begin{aligned}t_{\mathrm{PR}}^2\left(\mathbf{x}_{\mathrm{P}}^{\min}\right)=&\frac{1}{v_1^2}\left[\left(\frac{d}{2}-\frac{L\sin 2\varphi(v_2^2-v_1^2)}{2(v_1^2\sin^2\varphi+v_2^2\cos^2\varphi)}\right)\cos\varphi+L\sin\varphi\right]^2\\&+\frac{1}{v_2^2}\left[\left(\frac{d}{2}-\frac{L\sin 2\varphi(v_2^2-v_1^2)}{2(v_1^2\sin^2\varphi+v_2^2\cos^2\varphi)}\right)\sin\varphi-L\cos\varphi\right]^2.\end{aligned} \tag{19}$$

Following the same steps as before, we simplify the terms in brackets to obtain

$$t_{\mathrm{PR}}^2\left(\mathbf{x}_{\mathrm{P}}^{\min}\right)=\frac{1}{v_1^2}\left[\frac{d}{2}\cos\varphi+\frac{Lv_1^2\sin\varphi}{v_1^2\sin^2\varphi+v_2^2\cos^2\varphi}\right]^2+\frac{1}{v_2^2}\left[\frac{d}{2}\sin\varphi-\frac{Lv_2^2\cos\varphi}{v_1^2\sin^2\varphi+v_2^2\cos^2\varphi}\right]^2, \tag{20}$$

which can be further simplified as

$$t_{\mathrm{PR}}^2\left(\mathbf{x}_{\mathrm{P}}^{\min}\right)=\frac{d^2}{4v_1^2v_2^2}(v_1^2\sin^2\varphi+v_2^2\cos^2\varphi)+\frac{L^2}{v_1^2\sin^2\varphi+v_2^2\cos^2\varphi}=\frac{d^2}{4v^2(\theta=\pi/2)}+\frac{L^2v^2(\theta=\pi/2)}{v_1^2v_2^2}. \tag{21}$$

By comparing (21) to (18), we observe that

$$t_{\mathrm{SP}}\left(\mathbf{x}_{\mathrm{P}}^{\min}\right)=t_{\mathrm{PR}}\left(\mathbf{x}_{\mathrm{P}}^{\min}\right), \tag{22}$$

meaning that the fastest ray path is the path with equal traveltime along each segment. Taking this into account, we finally derive the analytical expression for first-arrival reflection traveltime:

$$t_{\mathrm{SR}}^2\left(\mathbf{x}_{\mathrm{P}}^{\min}\right)=4t_{\mathrm{SP}}^2\left(\mathbf{x}_{\mathrm{P}}^{\min}\right)=\frac{d^2}{v^2(\theta=\pi/2)}+\frac{4L^2v^2(\theta=\pi/2)}{v_1^2v_2^2}. \tag{23}$$

Note that (22) also means that the mirror image of the receiver, namely a virtual receiver $\tilde{R}$ located below the reflector that satisfies $t_{\mathrm{S\tilde{R}}}=t_{\mathrm{SR}}$, is generally located at

$$\mathbf{x}_{\tilde{\mathrm{R}}}=2\mathbf{x}_{\mathrm{P}}^{\min}-\mathbf{x}_{\mathrm{S}}. \tag{24}$$

V. Proof: accuracy of the reflection point

When deriving the reflection point expression, we assumed that this point is shifted from the source-receiver mid-point by the same constant δ for every source-receiver combination. If this assumption is accurate, the derivative of $t_{\mathrm{SR}}^2(\mathbf{x}_{\mathrm{P}})$ with respect to $\mathbf{x}_{\mathrm{P}}$ (or $x_{1,\mathrm{P}}$ since the reflection point is always at the reflector) will always be zero at $\mathbf{x}_{\mathrm{P}}^{\min}$ given by (12), i.e.,

$$\left.\frac{dt_{\mathrm{SR}}}{dx_{1,\mathrm{P}}}\right|_{\mathbf{x}_{\mathrm{P}}=\mathbf{x}_{\mathrm{P}}^{\min}}=\left.\frac{dt_{\mathrm{SP}}}{dx_{1,\mathrm{P}}}\right|_{\mathbf{x}_{\mathrm{P}}=\mathbf{x}_{\mathrm{P}}^{\min}}+\left.\frac{dt_{\mathrm{PR}}}{dx_{1,\mathrm{P}}}\right|_{\mathbf{x}_{\mathrm{P}}=\mathbf{x}_{\mathrm{P}}^{\min}}=0. \tag{25}$$

That is, Fermat's principle must be satisfied for any source-receiver combination. In the following, we prove that (25) always holds for $\mathbf{x}_{\mathrm{P}}^{\min}$ given by (12).

As before, we transform the derivatives in (25) using squared traveltimes as

$$\left.\frac{dt_{\mathrm{SR}}}{dx_{1,\mathrm{P}}}\right|_{\mathbf{x}_{\mathrm{P}}=\mathbf{x}_{\mathrm{P}}^{\min}}=\left.\left[\frac{1}{2t_{\mathrm{SP}}}\frac{dt_{\mathrm{SP}}^2}{dx_{1,\mathrm{P}}}+\frac{1}{2t_{\mathrm{PR}}}\frac{dt_{\mathrm{PR}}^2}{dx_{1,\mathrm{P}}}\right]\right|_{\mathbf{x}_{\mathrm{P}}=\mathbf{x}_{\mathrm{P}}^{\min}}=\frac{1}{2t_{\mathrm{SP}}(\mathbf{x}_{\mathrm{P}}^{\min})}\left.\left[\frac{dt_{\mathrm{SP}}^2}{dx_{1,\mathrm{P}}}+\frac{dt_{\mathrm{PR}}^2}{dx_{1,\mathrm{P}}}\right]\right|_{\mathbf{x}_{\mathrm{P}}=\mathbf{x}_{\mathrm{P}}^{\min}}=0. \tag{26}$$

The last step uses the equality given in (22). Therefore, this equation is satisfied when

$$\left.\frac{dt_{\mathrm{SP}}^2}{dx_{1,\mathrm{P}}}\right|_{\mathbf{x}_{\mathrm{P}}=\mathbf{x}_{\mathrm{P}}^{\min}}=-\left.\frac{dt_{\mathrm{PR}}^2}{dx_{1,\mathrm{P}}}\right|_{\mathbf{x}_{\mathrm{P}}=\mathbf{x}_{\mathrm{P}}^{\min}}. \tag{27}$$

To see if this is true, we compute both derivatives:

1) Derivative of t_{SP}^2 at $\mathbf{x}_{\mathrm{P}}^{\min}$:

$$\left.\frac{dt_{\mathrm{SP}}^2}{dx_{1,\mathrm{P}}}\right|_{\mathbf{x}_{\mathrm{P}}=\mathbf{x}_{\mathrm{P}}^{\min}}=\left.\frac{2\cos\varphi}{v_1^2}\left[(x_{1,\mathrm{P}}-x_{1,\mathrm{S}})\cos\varphi-L\sin\varphi\right]+\frac{2\sin\varphi}{v_2^2}\left[(x_{1,\mathrm{P}}-x_{1,\mathrm{S}})\sin\varphi+L\cos\varphi\right]\right|_{\mathbf{x}_{\mathrm{P}}=\mathbf{x}_{\mathrm{P}}^{\min}}. \tag{28}$$

Here, we can use (17) to simplify the terms in brackets after evaluating them at $\mathbf{x}_{\mathrm{P}}^{\min}$:

$$\left.\frac{dt_{\mathrm{SP}}^2}{dx_{1,\mathrm{P}}}\right|_{\mathbf{x}_{\mathrm{P}}=\mathbf{x}_{\mathrm{P}}^{\min}}=\frac{2\cos\varphi}{v_1^2}\left[\frac{d}{2}\cos\varphi-\frac{Lv_1^2\sin\varphi}{v_1^2\sin^2\varphi+v_2^2\cos^2\varphi}\right]+\frac{2\sin\varphi}{v_2^2}\left[\frac{d}{2}\sin\varphi+\frac{Lv_2^2\cos\varphi}{v_1^2\sin^2\varphi+v_2^2\cos^2\varphi}\right], \tag{29}$$

which can be further simplified as

$$\left.\frac{dt_{\mathrm{SP}}^2}{dx_{1,\mathrm{P}}}\right|_{\mathbf{x}_\mathrm{P}=\mathbf{x}_\mathrm{P}^{\min}} = d\left(\frac{\cos^2\varphi}{v_1^2}+\frac{\sin^2\varphi}{v_2^2}\right). \tag{30}$$

2) Derivative of t_{PR}^2 at $\mathbf{x}_\mathrm{P}^{\min}$:

$$\left.\frac{dt_{\mathrm{PR}}^2}{dx_{1,\mathrm{P}}}\right|_{\mathbf{x}_\mathrm{P}=\mathbf{x}_\mathrm{P}^{\min}} = \left.\frac{-2\cos\varphi}{v_1^2}\left[(x_{1,\mathrm{R}}-x_{1,\mathrm{P}})\cos\varphi+L\sin\varphi\right]-\frac{2\sin\varphi}{v_2^2}\left[(x_{1,\mathrm{R}}-x_{1,\mathrm{P}})\sin\varphi-L\cos\varphi\right]\right|_{\mathbf{x}_\mathrm{P}=\mathbf{x}_\mathrm{P}^{\min}}. \tag{31}$$

As before, we can use (20) to simplify the terms in brackets after evaluating them at $\mathbf{x}_\mathrm{P}^{\min}$:

$$\left.\frac{dt_{\mathrm{PR}}^2}{dx_{1,\mathrm{P}}}\right|_{\mathbf{x}_\mathrm{P}=\mathbf{x}_\mathrm{P}^{\min}} = \frac{-2\cos\varphi}{v_1^2}\left[\frac{d}{2}\cos\varphi+\frac{Lv_1^2\sin\varphi}{v_1^2\sin^2\varphi+v_2^2\cos^2\varphi}\right]-\frac{2\sin\varphi}{v_2^2}\left[\frac{d}{2}\sin\varphi-\frac{Lv_2^2\cos\varphi}{v_1^2\sin^2\varphi+v_2^2\cos^2\varphi}\right], \tag{32}$$

which can be further simplified as

$$\left.\frac{dt_{\mathrm{PR}}^2}{dx_{1,\mathrm{P}}}\right|_{\mathbf{x}_\mathrm{P}=\mathbf{x}_\mathrm{P}^{\min}} = -d\left(\frac{\cos^2\varphi}{v_1^2}+\frac{\sin^2\varphi}{v_2^2}\right). \tag{33}$$

By comparing (30) and (33), we see that (27) is satisfied, meaning that the expression of the reflection point given in (12) is exact and does not involve any approximation.

VI. Reflector inclination: derivation of the reflection point

In this subsection, we calculate the reflection point for an experimental setup with an inclined reflector. To take advantage of our previous results, we use the equivalent experimental setup depicted in Fig. 1 and consider a virtual source $\tilde{S}$ with the same elevation as the receiver R. The horizontal distance between $\tilde{S}$ and the reflection point P is then given by

$$\tilde{x}_{1,\mathrm{P}} = x_{1,\mathrm{P}} + x = \frac{d\cos\alpha + x}{2} + \delta', \tag{34}$$

where

$$\delta' = \frac{(L+d\sin\alpha)\sin 2\varphi(v_2^2-v_1^2)}{2(v_1^2\sin^2\varphi+v_2^2\cos^2\varphi)}. \tag{35}$$

The last step uses our previous result in (12). From here, we see that the horizontal distance between the actual source S and the reflection point P is

$$x_{1,\mathrm{P}} = \frac{d\cos\alpha - x}{2} + \delta'. \tag{36}$$

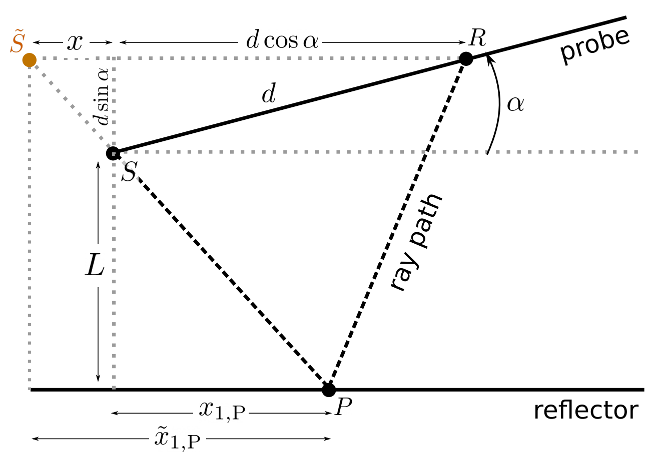

Fig. 1. Schematic illustration of the experimental setup with an inclined ultrasound probe by α and a horizontal reflector in front of it. This setup is equivalent to having an inclined reflector in front of a horizontally placed linear probe [see Fig. 3 in the main manuscript]. The vertical probe-reflector distance L is measured from the first transducer element, where in this example we locate the source S. R denotes the receiver located at a distance d from S, P is the reflection point, and $\tilde{S}$ is a virtual source with same elevation as R. The horizontal distance between $\tilde{S}$ and S is x. This virtual source will allow us to compute the reflection point using (12).

We can find a second relationship between x and $x_{1,\mathrm{P}}$ using the trigonometric identity

$$\frac{d\sin\alpha}{x} = \frac{L}{x_{1,\mathrm{P}}} \quad\Rightarrow\quad x = \frac{x_{1,\mathrm{P}}d\sin\alpha}{L}. \tag{37}$$

Finally, upon inserting (37) in (36), we obtain

$$x_{1,\mathrm{P}} = \frac{d\cos\alpha}{2} - \frac{x_{1,\mathrm{P}}\sin\alpha}{2L} + \delta' \quad \Rightarrow \quad x_{1,\mathrm{P}} = \frac{L(d\cos\alpha + 2\delta')}{2L + d\sin\alpha}. \tag{38}$$

We can generalize this expression by dropping the assumption that S is located at the origin of the coordinate system. Then, the reflection point becomes

$$x_{1,\mathrm{P}} = d_\mathrm{S}\cos\alpha + \frac{(L + d_\mathrm{S}\sin\alpha)(d\cos\alpha + 2\delta')}{2(L + d_\mathrm{S}\sin\alpha) + d\sin\alpha}, \tag{39}$$

with

$$\delta' = \frac{(L + d_\mathrm{S}\sin\alpha + d\sin\alpha)\sin 2\varphi(v_2^2 - v_1^2)}{2(v_1^2\sin^2\varphi + v_2^2\cos^2\varphi)}, \tag{40}$$

where d_S is the distance between the source and the origin of the coordinate system (i.e., the first transducer element of the probe).

VII. Reflector inclination: first-arrival reflection traveltime

For simplicity, we calculate the traveltime t_SR considering the mirror image of the receiver $\tilde{R}$. This virtual receiver is located below the reflector, where $t_{\mathrm{S}\tilde{\mathrm{R}}} = t_\mathrm{SR}$ is satisfied. When the reflector is not inclined, the location of the virtual receiver is given by (24). In our example, therefore, this location is $\mathbf{x}_{\tilde{\mathrm{R}}} = (2\tilde{x}_{1,\mathrm{P}} - x, 2L + d\sin\alpha) = (d\cos\alpha + 2\delta', 2L + d\sin\alpha)$, shown in Fig. 2. Note that we again place the origin of the coordinate system at S.

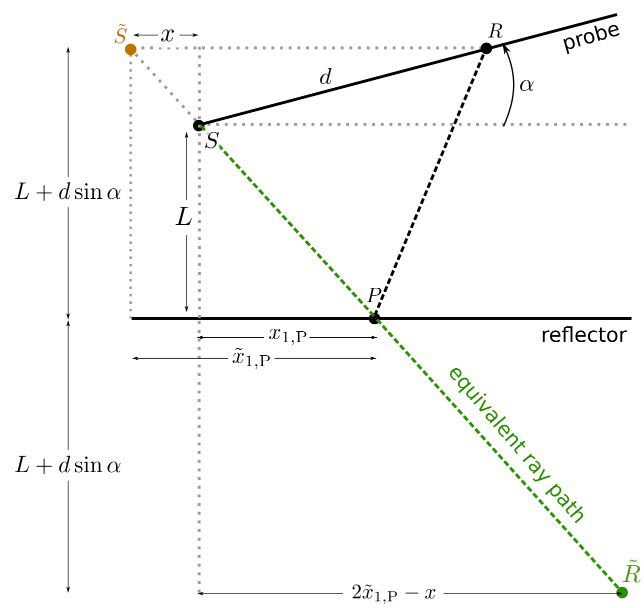

Fig. 2. Schematic illustration showing the location of the mirror image $\tilde{R}$ of the receiver R. The traveltime of a straight ray traveling from S to $\tilde{R}$ (green dashed line) is the same as the first-arrival reflection traveltime from S to R, that is, $t_{\mathrm{S}\tilde{\mathrm{R}}} = t_\mathrm{SR}$. This virtual receiver is located at $\mathbf{x}_{\tilde{\mathrm{R}}} = (2\tilde{x}_{1,\mathrm{P}} - x, 2L + d\sin\alpha)$ with the origin of the coordinate system at S. We refer the reader to Fig. 1 to understand the meaning of the rest of the symbols in the image.

Following (5), the traveltime between S and $\tilde{R}$ is given by

$$t_{\mathrm{S}\tilde{\mathrm{R}}}^2 = \frac{1}{v_1^2}\underbrace{\left[(d\cos\alpha + 2\delta')\cos\varphi - (2L + d\sin\alpha)\sin\varphi\right]^2}_{\mathrm{I}^2} + \frac{1}{v_2^2}\underbrace{\left[(d\cos\alpha + 2\delta')\sin\varphi + (2L + d\sin\alpha)\cos\varphi\right]^2}_{\mathrm{II}^2}. \tag{41}$$

To simplify this expression, we first simplify the terms in brackets separately using the definition of δ' in (35):

1) The first term can be reduced to

$$\mathrm{I} = d\cos(\varphi + \alpha) + \frac{d\sin\alpha\sin 2\varphi\cos\varphi(v_2^2 - v_1^2) - 2Lv_1^2\sin\varphi}{v_1^2\sin^2\varphi + v_2^2\cos^2\varphi}. \tag{42}$$

After taking the square of this term and dividing it with v_1^2, we obtain

$$\begin{aligned}\frac{\mathrm{I}^2}{v_1^2} = \frac{d^2\cos^2(\varphi+\alpha)}{v_1^2} &+ 4d\sin\varphi\cos(\varphi+\alpha)\frac{\left(d\sin\alpha\cos^2\varphi\left(\frac{v_2^2 - v_1^2}{v_1^2}\right) - L\right)}{v_1^2\sin^2\varphi + v_2^2\cos^2\varphi} \\ &+ \frac{d^2\sin^2\alpha\sin^2 2\varphi\cos^2\varphi\left(\frac{v_2^2 - v_1^2}{v_1}\right)^2 - 2Ld\sin\alpha\sin^2 2\varphi(v_2^2 - v_1^2) + 4L^2v_1^2\sin^2\varphi}{(v_1^2\sin^2\varphi + v_2^2\cos^2\varphi)^2}.\end{aligned} \tag{43}$$

2) The second term can be reduced to

$$\mathrm{II} = d\sin(\varphi+\alpha) + \frac{d\sin\alpha\sin 2\varphi\sin\varphi(v_2^2-v_1^2)+2Lv_2^2\cos\varphi}{v_1^2\sin^2\varphi+v_2^2\cos^2\varphi}. \tag{44}$$

As before, we take the square of II and divide it with v_2^2 to obtain

$$\begin{aligned}\frac{\mathrm{II}^2}{v_2^2} = \frac{d^2\sin^2(\varphi+\alpha)}{v_2^2} &+ 4d\cos\varphi\sin(\varphi+\alpha)\frac{\left(d\sin\alpha\sin^2\varphi\left(\frac{v_2^2-v_1^2}{v_2^2}\right)+L\right)}{v_1^2\sin^2\varphi+v_2^2\cos^2\varphi} \\ &+ \frac{d^2\sin^2\alpha\sin^2 2\varphi\sin^2\varphi\left(\frac{v_2^2-v_1^2}{v_2}\right)^2+2Ld\sin\alpha\sin^2 2\varphi(v_2^2-v_1^2)+4L^2v_2^2\cos^2\varphi}{(v_1^2\sin^2\varphi+v_2^2\cos^2\varphi)^2}.\end{aligned} \tag{45}$$

We notice that (43) and (45) have common terms that will vanish when we sum them to calculate $t^2_{\mathrm{S\tilde{R}}}$. Moreover, using the symmetries between their terms, we can express the traveltime as

$$\begin{aligned}t^2_{\mathrm{S\tilde{R}}} =\ & d^2\left(\frac{\sin^2(\varphi+\alpha)}{v_2^2}+\frac{\cos^2(\varphi+\alpha)}{v_1^2}\right) \\ &+ \frac{4Ld\sin\alpha - d^2\sin^2\alpha\sin^2 2\varphi\frac{(v_1^2-v_2^2)^2}{v_1^2v_2^2}}{v_1^2\sin^2\varphi+v_2^2\cos^2\varphi} + d^2\sin 2\alpha\sin 2\varphi\frac{v_2^2-v_1^2}{v_1^2v_2^2} \\ &+ \frac{4L^2+d^2\sin^2\alpha\sin^2 2\varphi\frac{(v_2^2-v_1^2)^2}{v_1^2v_2^2}}{v_1^2\sin^2\varphi+v_2^2\cos^2\varphi},\end{aligned} \tag{46}$$

where each line in this equation refers to one term in (43) and (45), following the same order. We can futher simplify (46) as

$$\begin{aligned}t^2_{\mathrm{S\tilde{R}}} =\ & d^2\left(\frac{\sin^2(\varphi+\alpha)}{v_2^2}+\frac{\cos^2(\varphi+\alpha)}{v_1^2}\right) \\ &+ \frac{4L(L+d\sin\alpha)}{v_1^2\sin^2\varphi+v_2^2\cos^2\varphi} + d^2\sin 2\alpha\sin 2\varphi\frac{v_2^2-v_1^2}{v_1^2v_2^2}.\end{aligned} \tag{47}$$

Here, the sum of the first and third term equals to

$$d^2\left(\frac{\sin^2(\varphi+\alpha)}{v_2^2}+\frac{\cos^2(\varphi+\alpha)}{v_1^2}\right) + d^2\sin 2\alpha\sin 2\varphi\frac{v_2^2-v_1^2}{v_1^2v_2^2} = \frac{d^2}{v_1^2v_2^2}\left(v_1^2\sin^2(\varphi-\alpha)+v_2^2\cos^2(\varphi-\alpha)\right). \tag{48}$$

Therefore, the traveltime $t^2_{\mathrm{S\tilde{R}}}$, which is equal to t^2_{SR}, reduces to

$$t^2_{\mathrm{SR}} = \frac{d^2}{v_1^2v_2^2}\left(v_1^2\sin^2(\varphi-\alpha)+v_2^2\cos^2(\varphi-\alpha)\right) + \frac{4L(L+d\sin\alpha)}{v_1^2\sin^2\varphi+v_2^2\cos^2\varphi}. \tag{49}$$

So far, we have considered the experimental setup depicted in Figs. 1 and 2. However, this setup is a rotated version of the actual experimental configuration considered in the main manuscript, as shown in Fig. 3. To find an expression for the traveltime that is valid for our original experimental setup, we need to apply the transformations $L \to L\cos\alpha$ and $\varphi \to \varphi+\alpha$. The transformation for L considers the case in which the source is located at the first transducer element (origin of the coordinate system). We can generalize the traveltimes to any source location applying the transformation $L \to L\cos\alpha + d_{\mathrm{S}}\sin\alpha$, where d_{S} is the distance between S and the origin of the coordinate system. Thus, the first-arrival reflection traveltime between S and R becomes

$$t^2_{\mathrm{SR}} = \frac{d^2}{v^2(\pi/2)} + \frac{4L'(L'+d\sin\alpha)}{v_1^2\sin^2(\varphi+\alpha)+v_2^2\cos^2(\varphi+\alpha)} \tag{50}$$

with

$$L' = L\cos\alpha + d_{\mathrm{S}}\sin\alpha. \tag{51}$$

VIII. Constraining anisotropy parameters

In this section, we show additional figures to clarify the content of Fig. 4 in the main manuscript. This figure represents the equivalent models in terms of the anisotropy angle and the velocity ratio. This is useful to visualize three-dimensional models in a two-dimensional image. However, it may not be clear whether each point in this figure corresponds to a single anisotropy model or a set of models with equal velocity ratio. In order to clarify this point, we show two additional figures of the same result. Figure 4(a) shows the parameters φ and v_1 of the models, whereas Figure 4(b) shows φ and v_1. We can see that each point in Fig. 4 of the main manuscript and the intersection point of the curves represent a single anisotropy model.

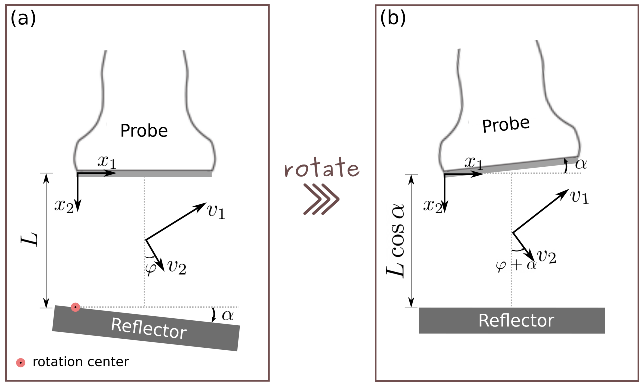

Fig. 3. Schematic illustration showing two equivalent experimental setups. (a) Our original setup considers the reflector inclined by α with respect to the x_1-axis. The vertical distance between the first transducer element (origin of the coordinate system) and the reflector is L. The anisotropy symmetry axis of the medium has the orientation φ with respect to the x_2-axis. (b) We rotate the whole system by α in order to imagine an equivalent setup with no reflector inclination. Now, the probe is inclined with respect to the x_1-axis, the anisotropy of the medium has the orientation $\varphi + \alpha$, and the vertical probe-reflector distance becomes $L \cos \alpha$.

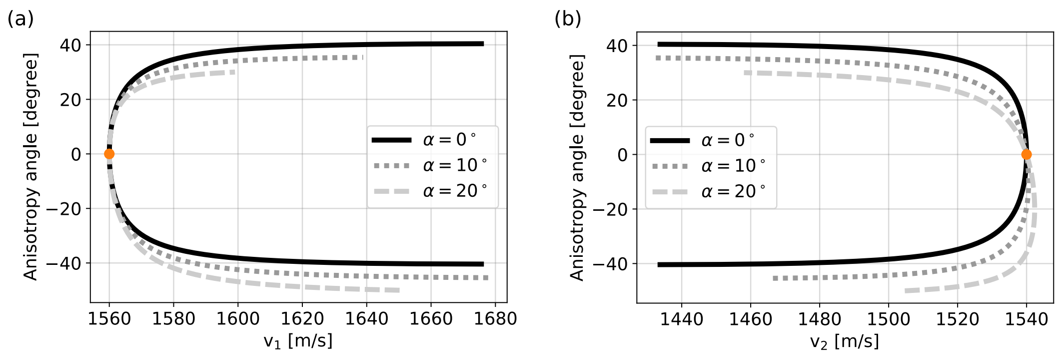

Fig. 4. Figures corresponding to the result shown in Fig. 4 of the main manuscript. We show muscle models equivalent to $\hat{\mathbf{m}} = (1560 \text{ m/s}, 1540 \text{ m/s}, 0°)$ (orange) in terms of first-arrival reflection traveltimes using reflector inclination angles $\alpha = 0°, 10°$, and $20°$. Each model is defined by three parameters: anisotropy angle φ and velocities v_1 and v_2. For visualization, we show in (a) the parameters φ and v_1 of the models and in (b) the parameters φ and v_2 of the same models. We can observe that the three curves intersect in a single point that represents $\hat{\mathbf{m}}$.

IX. Extended Bayesian formulation for uncertain reflector inclination angles

In this section, we show numerical examples supporting the uniqueness of the solution shown in Fig. 9(b) (in gray) of the main manuscript. We use the same Bayesian formulation that considers inclination angles as unknown model parameters and perform the inversion initializing the Metropolis-Hastings Markov chain Monte Carlo (MCMC) algorithm with models that deviate strongly from the true model $\mathbf{m}_{\text{true}} = (1560 \text{ m/s}, 1540 \text{ m/s}, 0°, 0°, 5°)$. This allows us to explore a wider area of the model space and converge to other maxima of the posterior probability density function, if any. Figs. 5–7 show the results obtained when the MCMC is initialized with models $\mathbf{m}_{\text{init}} = (1350 \text{ m/s}, 1350 \text{ m/s}, 40°, 10°, 15°)$, $\mathbf{m}_{\text{init}} = (1750 \text{ m/s}, 1750 \text{ m/s}, -40°, 15°, 15°)$, $\mathbf{m}_{\text{init}} = (1750 \text{ m/s}, 1750 \text{ m/s}, 40°, 15°, 0°)$, $\mathbf{m}_{\text{init}} = (1310 \text{ m/s}, 1310 \text{ m/s}, -40°, 15°, 0°)$, $\mathbf{m}_{\text{init}} = (1310 \text{ m/s}, 1750 \text{ m/s}, 40°, 5°, 0°)$, and $\mathbf{m}_{\text{init}} = (1750 \text{ m/s}, 1310 \text{ m/s}, -40°, 5°, 0°)$. Note that parameter values chosen for these initial models are close to the extreme limits imposed by our uniform priors, which are defined within the range of $[1300 \text{ m/s}, 1800 \text{ m/s}]$ and $[-45°, 45°)$ for velocities and the anisotropy angle, respectively. Yet, all MCMC realizations converge to the same maximum of the posterior as in Fig. 9(b) (gray), suggesting that the solution uniqueness is still given within the model subspace defined by the priors in this extended Bayesian formulation.

X. Phase velocities in elliptically anisotropic media

The Christoffel equation relates the stiffness tensor c_{ijkl} to the phase velocities V as

$$\det[c_{ijkl} n_i n_l - \rho V^2 \delta_{jk}] = 0, \tag{52}$$

where the Einstein summation convention is implied for repeated indices. Here, ρ denotes medium density, δ_{jk} is the Kronecker delta, and n_i refers to the ith component of the wavefront normal vector. If we assume the muscle as an elliptically anisotropic medium, the stiffness tensor will have only three relevant components, which are $c_{1111} \equiv c_{11}$, $c_{1122} \equiv c_{12}$, and $c_{2222} \equiv c_{22}$ in Voigt notation.

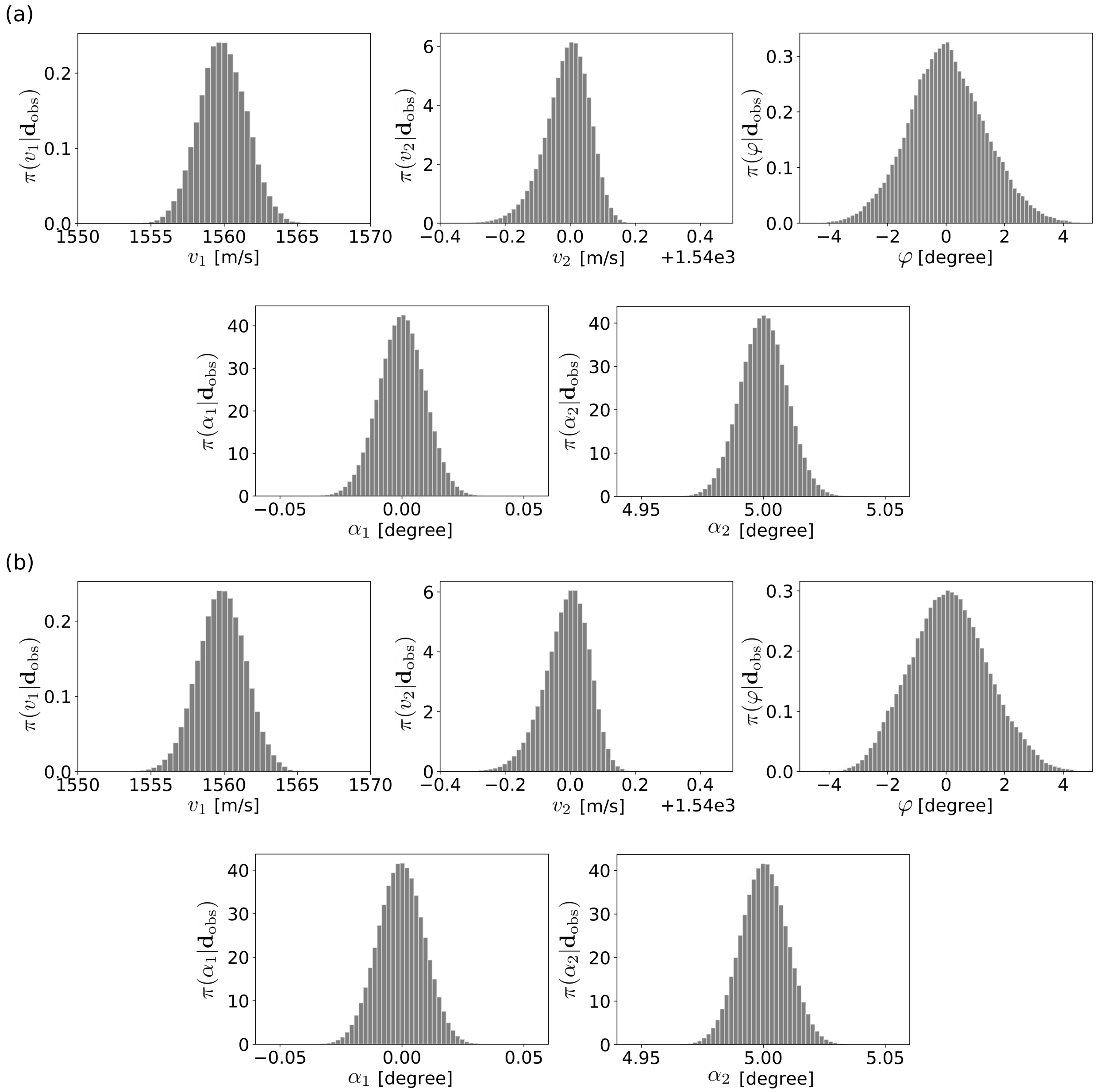

Fig. 5. Marginal probability density functions obtained when we initialize the Metropolis-Hastings Markov chain Monte Carlo algorithm with models (a) $\mathbf{m}_{\text{init}} = (1350 \text{ m/s}, 1350 \text{ m/s}, 40^\circ, 10^\circ, 15^\circ)$ and (b) $\mathbf{m}_{\text{init}} = (1750 \text{ m/s}, 1750 \text{ m/s}, -40^\circ, 15^\circ, 15^\circ)$.

We consider a two-dimensional problem defined in the x_1x_2-plane. For an arbitrary wavefront direction $\mathbf{n} = (\sin\phi, \cos\phi)$, the determinant in (52) reduces to

$$\begin{vmatrix} c_{11}\sin^2\phi - \rho V^2 & c_{12}\sin\phi\cos\phi \\ c_{12}\sin\phi\cos\phi & c_{22}\cos^2\phi - \rho V^2 \end{vmatrix} = \rho^2 V^4 - \rho V^2 (c_{11}\sin^2\phi + c_{22}\cos^2\phi) + (c_{11}c_{22} - c_{12}^2)\sin^2\phi\cos^2\phi. \tag{53}$$

Following (52), we equate (53) to zero. This gives a second order polynomial for ρV^2 with solutions

$$\rho V^2 = \frac{1}{2}\left[(c_{11}\sin^2\phi + c_{22}\cos^2\phi) \pm \sqrt{(c_{11}\sin^2\phi + c_{22}\cos^2\phi)^2 - 4(c_{11}c_{22} - c_{12}^2)\sin^2\phi\cos^2\phi}\right]. \tag{54}$$

Here we can simplify the term inside the square root as

$$\rho V^2 = \frac{1}{2}\left[(c_{11}\sin^2\phi + c_{22}\cos^2\phi) \pm \sqrt{(c_{11}\sin^2\phi - c_{22}\cos^2\phi)^2 + c_{12}^2\sin^2 2\phi}\right]. \tag{55}$$

In general, only the positive sign guarantees a solution for V. Thus, the phase velocity of longitudinal waves is given by

$$V^2(\phi) = \frac{1}{2\rho}\left[c_{11}\sin^2\phi + c_{22}\cos^2\phi + G(\phi)\right] \tag{56}$$

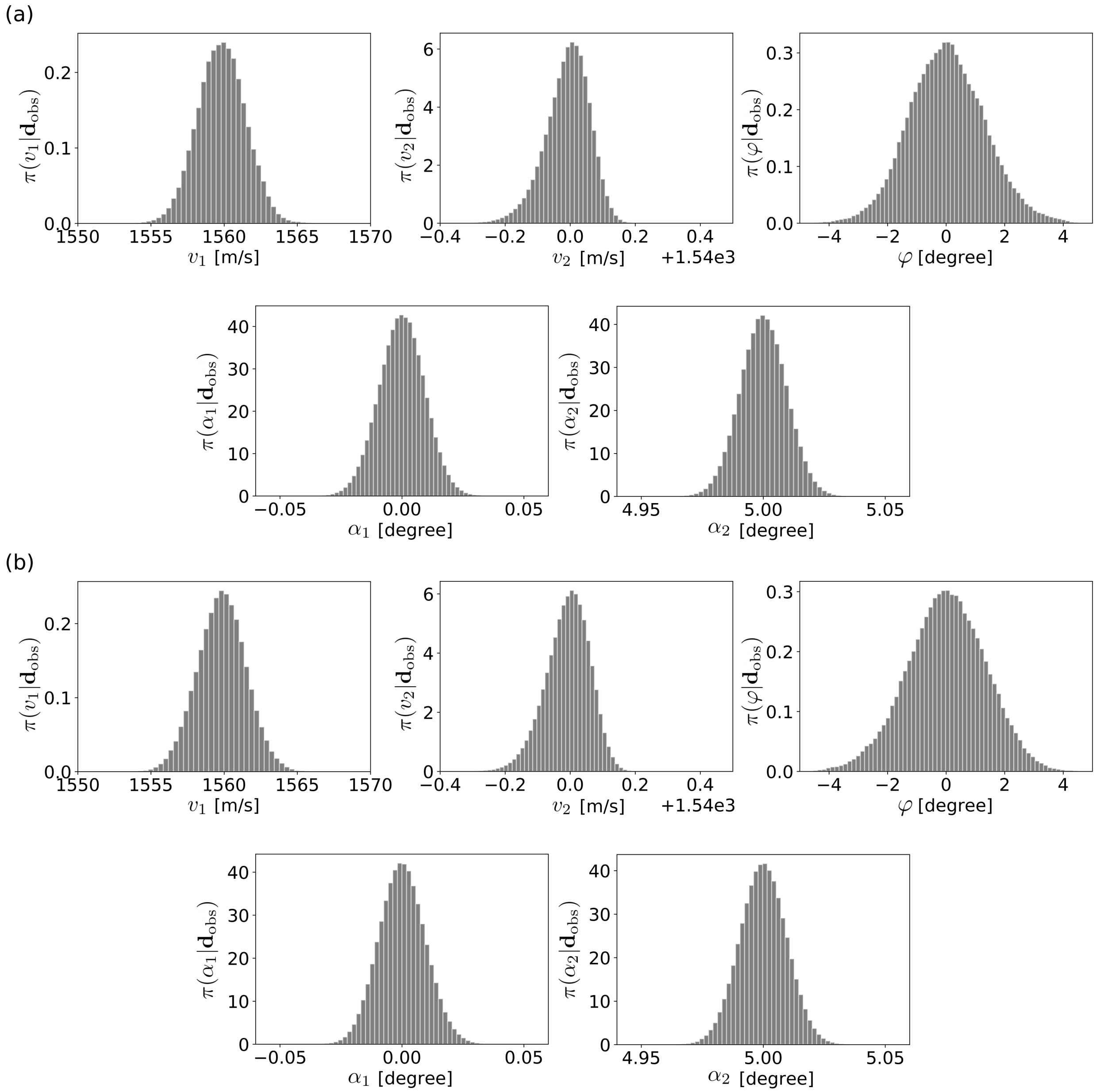

Fig. 6. Marginal probability density functions obtained when we initialize the Metropolis-Hastings Markov chain Monte Carlo algorithm with models (a) $\mathbf{m}_{\text{init}} = (1750 \text{ m/s}, 1750 \text{ m/s}, 40°, 15°, 0°)$ and (b) $\mathbf{m}_{\text{init}} = (1310 \text{ m/s}, 1310 \text{ m/s}, -40°, 15°, 0°)$.

with

$$G(\phi) = \left[\left(c_{11}\sin^2\phi - c_{22}\cos^2\phi\right)^2 + c_{12}^2\sin^2 2\phi\right]^{\frac{1}{2}}. \tag{57}$$

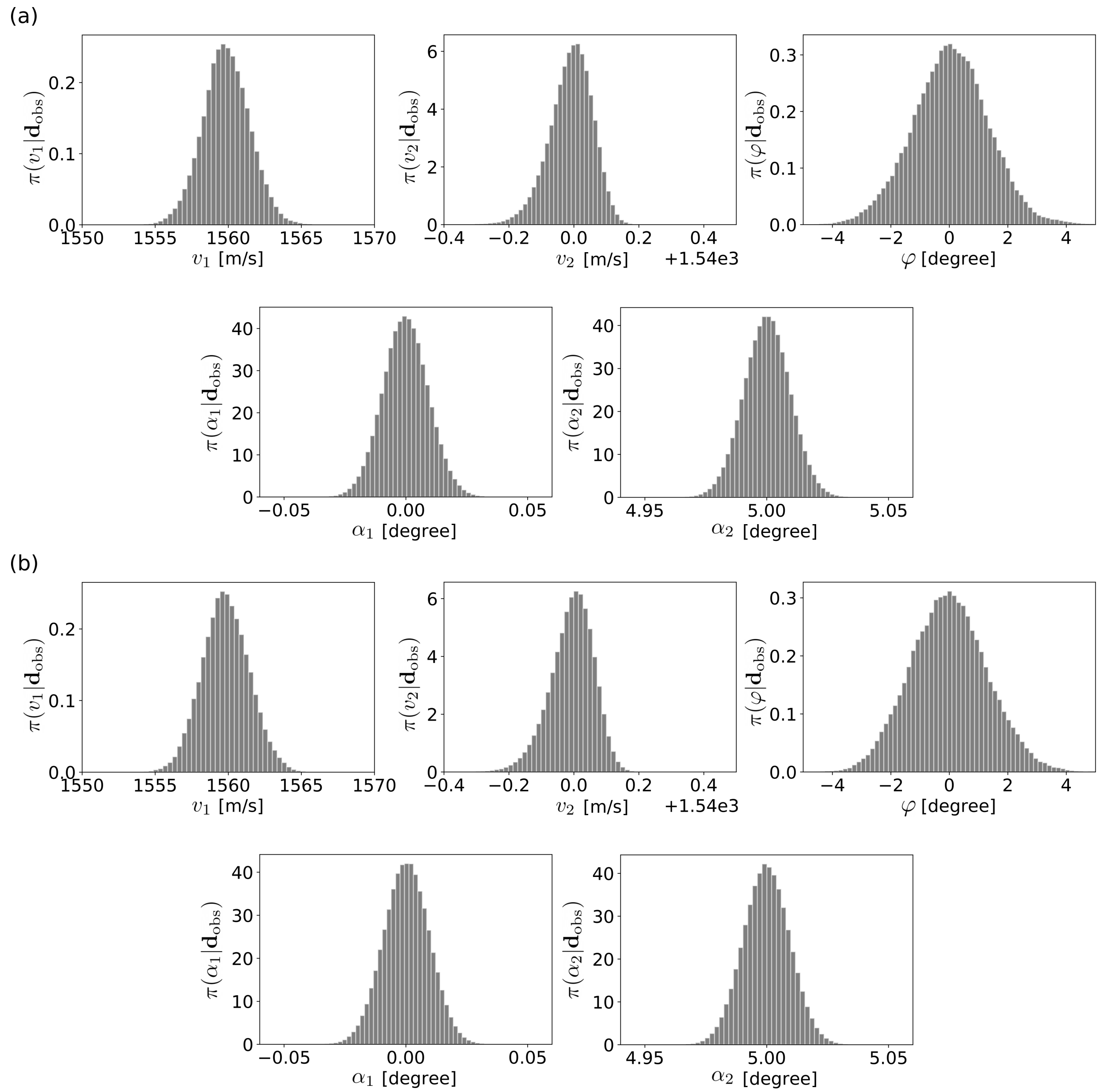

Fig. 7. Marginal probability density functions obtained when we initialize the Metropolis-Hastings Markov chain Monte Carlo algorithm with models (a) $\mathbf{m}_{\text{init}} = (1310 \text{ m/s}, 1750 \text{ m/s}, 40^\circ, 5^\circ, 0^\circ)$ and (b) $\mathbf{m}_{\text{init}} = (1750 \text{ m/s}, 1310 \text{ m/s}, -40^\circ, 5^\circ, 0^\circ)$.